# Resolving weather fronts increases the large-scale circulation response to Gulf Stream SST anomalies in variable-resolution CESM2 simulations

**Robert C. J. Wills[1,2], Adam R. Herrington[2], Isla R. Simpson[2], David S. Battisti[3]**

[1]Institute of Atmospheric and Climate Science, ETH Zurich, Switzerland
[2]NSF National Center for Atmospheric Research, Boulder, CO
[3]Department of Atmospheric Sciences, University of Washington, Seattle, WA

**Key Points:**

- There is a large circulation response to idealized Gulf Stream SST anomalies in an atmospheric model with 14-km regional grid refinement
- This response is weaker or absent in simulations with 28-km or coarser resolution, which do not fully resolve mesoscale frontal processes
- Transient-eddy fluxes of heat and momentum are modified as fronts pass over warm SSTs, leading to a large-scale circulation response

Corresponding author: Robert C. Jnglin Wills, `r.jnglinwills@usys.ethz.ch`

**Abstract**

Canonical understanding based on general circulation models (GCMs) is that the atmospheric circulation response to midlatitude sea-surface temperature (SST) anomalies is weak compared to the larger influence of tropical SST anomalies. However, the ∼100-km horizontal resolution of modern GCMs is too coarse to resolve strong updrafts within weather fronts, which could provide a pathway for surface anomalies to be communicated aloft. Here, we investigate the large-scale atmospheric circulation response to idealized Gulf Stream SST anomalies in Community Atmosphere Model (CAM6) simulations with 14-km regional grid refinement over the North Atlantic, and compare it to the responses in simulations with 28-km regional refinement and uniform 111-km resolution. The highest resolution simulations show a large positive response of the wintertime North Atlantic Oscillation (NAO) to positive SST anomalies in the Gulf Stream, a 0.4-standard-deviation anomaly in the seasonal-mean NAO for 2°C SST anomalies. The lower-resolution simulations show a weaker response with a different spatial structure. The enhanced large-scale circulation response results from an increase in resolved vertical motions with resolution and an associated increase in the influence of SST anomalies on transient-eddy heat and momentum fluxes in the free troposphere. In response to positive SST anomalies, these processes lead to a stronger and less variable North Atlantic jet, as is characteristic of positive NAO anomalies. Our results suggest that the atmosphere responds differently to midlatitude SST anomalies in higher-resolution models and that regional refinement in key regions offers a potential pathway to improve multi-year regional climate predictions based on midlatitude SSTs.

## Plain Language Summary

Variations in the ocean surface temperature (SST) influence the atmospheric circulation and thus climate over land. Canonical understanding is that tropical SSTs are more important than SSTs in midlatitudes. However, this understanding is based on climate models that don't resolve processes at scales less than 100 km. Here, we show that by increasing the atmospheric model resolution to resolve features on smaller scales, such as weather fronts, we find a larger atmospheric circulation response to midlatitude SST anomalies in the North Atlantic. North Atlantic SST anomalies can be predicted multiple years in advance, and a larger atmospheric circulation response to these predictable SST anomalies therefore implies increased predictability of climate over the surrounding land regions.

## 1 Introduction

North Atlantic sea-surface temperatures (SSTs) exhibit variability on seasonal to decadal timescales (e.g., Deser & Blackmon, 1993; R. Zhang et al., 2019), providing a potential source of predictability for atmospheric circulation and regional climate on these timescales. Recent work has improved our understanding of the ocean-atmosphere mechanisms governing North Atlantic SST variability (Menary et al., 2015; Delworth et al., 2017; S. Yeager & Robson, 2017; R. C. J. Wills et al., 2019; R. Zhang et al., 2019; Årthun et al., 2021) and shown that initialized climate models have skill in predicting the decadal evolution of North Atlantic SST (Msadek et al., 2014; Meehl et al., 2014; S. G. Yeager et al., 2018; D. Smith et al., 2019; Borchert et al., 2021; S. G. Yeager et al., 2023), but this will only help to make model-based predictions of regional climate anomalies in the surrounding continents if the models correctly simulate the atmospheric response to North Atlantic SST anomalies.

There is a large literature that tries to diagnose the atmospheric circulation response to North Atlantic SST anomalies from observations (see, e.g., Czaja & Frankignoul, 1999; Frankignoul et al., 2001; Czaja & Frankignoul, 2002; Gastineau et al., 2013; Gastineau & Frankignoul, 2015; S. M. Wills et al., 2016). However, the North Atlantic atmospheric

circulation exhibits strong internal variability, particularly due to the North Atlantic Oscillation (NAO), and this internal variability leads to a large intrinsic uncertainty in the diagnosed relationship between SSTs and circulation. The relationship between SSTs and circulation can be accurately diagnosed in climate model ensembles by averaging the relationship over a large number of simulations with different initial conditions, but the modeled relationship may not accurately reflect the real-world relationship. Indeed, while the canonical understanding based on climate models is that the large-scale circulation responds only weakly to midlatitude SST anomalies (Lau & Nath, 1994; Kushnir et al., 2002), there is growing evidence that the atmospheric response to midlatitude SST anomalies is systematically underestimated in climate models (Simpson et al., 2018, 2019; R. C. J. Wills et al., 2019; Czaja et al., 2019), and that this may be rectified by increasing the atmospheric resolution to resolve mesoscale processes over ocean frontal zones (Smirnov et al., 2015; Sheldon et al., 2017; Czaja et al., 2019; Oldenburg et al., 2022; Famooss Paolini et al., 2022; Seo et al., 2023).

Global climate models (GCMs) are typically run with ∼100 km or coarser horizontal resolution and are therefore unable to simulate mesoscale atmospheric processes such as the conditional symmetric instability and other frontal dynamics (∼10-100 km scales), which are important in the dynamics of weather. Increasing atmospheric model resolution is known to increase the strength of resolved updrafts (Jeevanjee & Romps, 2016; Herrington & Reed, 2018, 2020), including the ascent within weather fronts passing over the Gulf Stream SST front (Sheldon et al., 2017). It is well established that a deeper midlatitude heating anomaly will induce a larger downstream circulation response (Hoskins & Karoly, 1981), so if weather fronts could facilitate upward heat transport, this would lead to a larger circulation response. However, the influence of resolving updrafts on large-scale atmosphere-ocean coupling and seasonal-to-decadal predictability has not been systematically studied in climate models. A key factor limiting understanding is that current global high-resolution atmospheric modeling efforts on climate timescales (i.e., run for at least 10 years) are generally limited to $1/4°$ (∼25 km) atmospheric resolution (Bacmeister et al., 2014; Haarsma et al., 2016; Chang et al., 2020), which is still too coarse to fully resolve weather fronts. It is extremely costly to run global models at sub-25-km atmospheric resolution for the multiple decades needed to evaluate potential increases in the circulation response to midlatitude SST anomalies and in predictability at seasonal-to-decadal timescales.

In this work, we use variable-resolution (VR) simulations, where horizontal resolution is enhanced only in a region of interest, to evaluate the potential benefit of resolving mesoscale processes for atmospheric predictability stemming from persistent midlatitude SSTs. VR modeling is widely used in weather forecasting (e.g., Buizza et al. (2007)), but it is only starting to be explored for simulating climate variability and change (e.g., Zarzycki & Jablonowski, 2014; Zarzycki et al., 2015; van Kampenhout et al., 2019; Herrington et al., 2022; Wijngaard et al., 2023; Schemm, 2023). Here, we use VR configurations of the spectral element dynamical core in the Community Atmosphere Model (CAM-SE; P. H. Lauritzen et al., 2018), with 14-km ($\sim 1/8°$) or 28-km ($\sim 1/4°$) resolution over the North Atlantic and Europe (Fig. 1), to model the large-scale atmospheric circulation response to idealized North Atlantic SST anomalies. More details of the model and grid configuration are provided in Sections 2.1 and 2.2, respectively.

In this paper, we focus on simulations with idealized SST anomalies in the Gulf Stream region (Fig. 2; more details in Section 2.3). The Gulf Stream region is chosen due to the large magnitude of observed SST variability in this region (S. M. Wills et al., 2016) and the number of previous idealized modeling studies focusing on this region (Kaspi & Schneider, 2011; Kuwano-Yoshida et al., 2010; O'Reilly et al., 2017; Sheldon et al., 2017). Importantly, we use the same 1° resolution SSTs in all simulations, such that differences in the atmospheric response between grids are only due to differences in atmospheric resolution. There is an extensive literature documenting how climatological SST biases (Chang

119 et al., 2020; Athanasiadis et al., 2022; Oldenburg et al., 2022) and boundary layer pro-
120 cesses over midlatitude fronts (Small et al., 2014; Seo et al., 2023) improve with ocean-
121 model resolution. We leave aside the important influence of ocean resolution for this study
122 in order to isolate the influence of atmospheric resolution. Follow up work should inves-
123 tigate how simultaneously resolving mesoscale processes in the atmosphere and ocean
124 influences the simulation of large-scale atmosphere-ocean coupling.

125 The paper is organized as follows. Details of the model used, the new variable-resolution
126 grids, and the idealized SST anomaly simulations are described in Section 2. The results
127 of these simulations are shown in Section 3, including subsections on the large-scale cir-
128 culation response, the projection of the response onto modes of internal variability, the
129 local air-sea interactions and cross-front circulation response, a thermodynamic analy-
130 sis, and the modification of transient eddy fluxes by the SST forcing. In Section 4, we
131 summarize our findings and discuss the implications for the signal-to-noise paradox and
132 seasonal-to-decadal predictability.

## 2 Variable-Resolution Simulations

### 2.1 Modeling Setup

135 Our simulations use the Community Earth System Model version 2.2 (Danabasoglu
136 et al., 2020; Herrington et al., 2022). Specifically, they use the Community Atmospheric
137 Model version 6 (CAM6), with the spectral element (SE) dynamical core (P. H. Lauritzen
138 et al., 2018), coupled to a data ocean (specified SST and sea ice) and the Community
139 Land Model version 5 (Lawrence et al., 2019). The atmosphere has 32 hybrid pressure-
140 sigma levels in all simulations, with a model top at ∼2 hPa.

141 The CAM6 physical parameterization package (Gettelman et al., 2019) contains
142 a high-order turbulence closure, Cloud Layers Unified By Binormals (CLUBB; Golaz et
143 al., 2002; Bogenschutz et al., 2013), which serves as a boundary layer, shallow convec-
144 tion and cloud macrophysics scheme. CLUBB is sub-cycled with a two-moment cloud
145 microphysics scheme (Gettelman & Morrison, 2015; Gettelman et al., 2015) and aerosol
146 activation scheme (Liu et al., 2007) for simulating cloud-aerosol interactions and precip-
147 itation processes. Deep convection is parameterized using a convective quasi-equilibrium
148 mass flux scheme (G. Zhang & McFarlane, 1995; Neale et al., 2008), supporting down-
149 drafts and convective momentum transport (Richter & Rasch, 2008). Boundary layer
150 form drag is parameterized after Beljaars et al. (2004) and orographic gravity waves are
151 parameterized using an anisotropic scheme that utilizes sub-grid orientations of ridges
152 derived from a high-resolution gridded topography data set (Danielson & Gesch, 2011).

153 The SE dynamical core is based on a cube-sphere grid, tiled with quadrilateral finite-
154 elements. The hydrostatic primitive equations are solved using the continuous-Galerkin
155 method (Taylor et al., 1997; Taylor & Fournier, 2010), with each element containing a
156 2D fourth-order polynomial basis set, and with 4×4 quadrature nodes (i.e., grid points)
157 located at the roots of the basis functions. Grid points located on the element bound-
158 aries are shared with adjacent elements, facilitating communication between elements
159 via the direct stiffness summation (Canuto et al., 2007), and resulting in 3×3 indepen-
160 dent grid points per element. For quasi-uniform grids, the SE method for tracer trans-
161 port is replaced with the Conservative Semi-Lagrangian Multi-tracer transport scheme
162 (CSLAM; P. H. Lauritzen et al., 2017), which operates on a separate finite-volume grid
163 containing 3×3 control volumes per element. The physical parameterizations (hereafter
164 physics) are evaluated on the finite-volume grid in CSLAM, whereas in standard SE the
165 physics are evaluated at the quadrature points. A vertically Lagrangian scheme is used
166 in the vertical (Lin, 2004), wherein the 2D dynamics evolve in floating Lagrangian lay-
167 ers and are subsequently mapped back to a fixed Eulerian vertical grid.
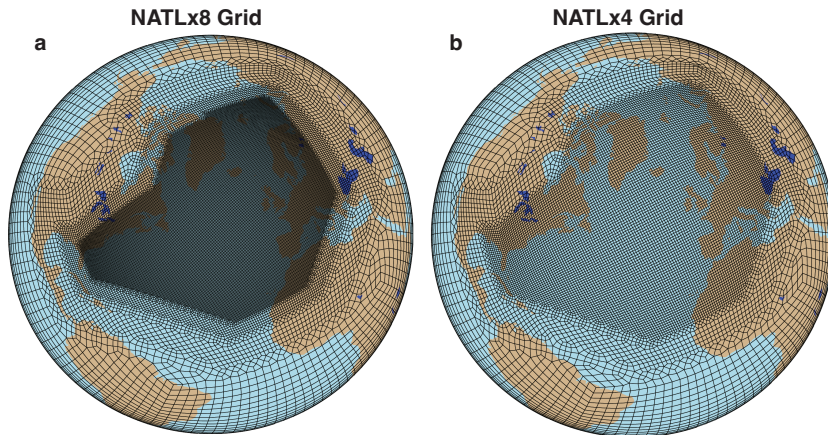
**Figure 1.** Variable-resolution North Atlantic grids for CAM-SE: (a) The NATLx8 grid, with horizontal resolution varying from 14 km resolution in the North Atlantic to 111 km in the far field; (b) the NATLx4 grid, with horizontal resolution varying from 28 km resolution in the North Atlantic to 111 km in the far field. Note that what is shown is the element grid; the computational grid has $3 \times 3$ independent grid points per element.

The SE dynamical core also supports variable-resolution grids, through invoking scale-aware hyper-viscosity (Guba et al., 2014) and imposing rougher terrain in the refined region, generated using CESM's topography generation software (P. Lauritzen et al., 2015). Variable-resolution currently does not support CSLAM, and the SE method is used for tracer transport instead. The parameterizations are otherwise unmodified as the refinement is increased. Notably, the deep convective parameterization is still included for the maximum refinement used in this study (14-km grid spacing in refinement region), though the convection scheme is known to become less active when the resolution is increased and the physics time-step is reduced (Williamson, 2013; Herrington & Reed, 2020). The SE time-stepping is reduced to satisfy the Courant-Friedrich-Lewy (CFL) condition in the refined region, whereas the time-stepping in the physics is reduced to avoid large time-truncation errors (Herrington & Reed, 2018). The physics time steps used are tabulated based on the grid spacing of the refinement region in Herrington et al. (2022).

### 2.2 North Atlantic Variable-Resolution Grids and Performance

The basis for our regionally refined grids is the quasi-uniform ne30pg3 grid (hereafter NE30), which has $30 \times 30$ quadrilateral elements per cubed sphere face and $3 \times 3$ control volumes per element, for a total of 48,600 control volumes and an average horizontal grid spacing of 111 km.

The North Atlantic (NATL) grids were generated using the software package SQuadgen (https://github.com/ClimateGlobalChange/squadgen) by rotating the cubed sphere to have a face in the center of the North Atlantic, then refining a region mostly within that face but extending also to neighboring faces (due to the irregular shape of the North Atlantic). The NATLx8 grid has a maximum of $8\times$ refinement, i.e., $8 \times 8$ elements in place of a single element in NE30, corresponding to a horizontal grid spacing of 14 km. This refinement takes places in 3 steps, with $2\times$ and $4\times$ refinement regions for transition between the $1\times$ region and the $8\times$ region. The NATLx4 grid simply replaces all $8\times$ regions with $4\times$ refinement, corresponding to a horizontal grid spacing of 28 km. The NATLx8 and NATLx4 grids have 317,567 and 142,346 control volumes, respectively.

The refinement region for our simulations includes the Gulf Stream, which is the primary region of focus for this work, but also extends to other regions of the North Atlantic. The rational for including some of these other regions of the North Atlantic is as follows. The southwest corner of the refinement region was chosen to contain the full Gulf Stream all the way from the Florida Straits. The southeast corner was chosen to include an important region of synoptic eddy wave breaking. The northwest corner was chosen to include the entirety of the Labrador Sea and Greenland. The northeast corner was chosen to simulate polar lows in the refinement region and to include important regions of sea-ice variability, the atmospheric response to which we plan to look at in subsequent work.

All simulations were performed on the Cheyenne Supercomputer (Computational and Information Systems Laboratory, 2019). Based on the known scaling behavior of variable-resolution CAM-SE (discussed in Herrington et al., 2022), we chose a relatively small number of nodes (30 nodes; 1080 cores) for the NATLx8 simulations for efficiency, because we were compute-time rather than throughput limited. The computational cost (including I/O) was approx. 71,000 core-hours per simulated year (CHPSY) for 50-day simulation segments, which completed in approx. 9 hours and were chosen to be under the 12-hour wall time. For NATLx4, the computational cost was approx. 21,500 CHPSY for 6-month simulation segments using 30 nodes, which completed in approx. 10 hours and were chosen to be under the 12-hours wall time. For NE30, the computational cost was approx. 1,900 CHPSY for 6-month simulation segments using 4 nodes, which completed in approx. 7 hours. We thus found that NATLx4 and NATLx8 have $11\times$ and $37\times$ increases in cost compared to NE30, respectively, where this includes I/O and the number of nodes used was changed according to what was practical. In total, approximately 10 million core-hours were used for the simulations in this paper. These simulations also serve the purpose of testing this new variable-resolution grid, with additional simulations forthcoming.

### 2.3 Idealized Specified-SST Experiments

For each grid (NATLx8, NATLx4, and NE30) we run a reference simulation with year-2000 radiative forcing, year-1850 land-use, and a specified seasonally varying SST climatology. The specified climatological SSTs and sea ice concentrations are computed from an average over years 1995-2005 in a merged dataset composed of the Hadley Center's SST/sea-ice version 1.1 and the NOAA Optimal Interpolation analysis version 2 (Hurrell et al., 2008). These boundary conditions are imposed at 1° spatial resolution and monthly time resolution and are interpolated to the atmospheric-model grid and daily time resolution by the CESM coupler. All simulations are started from January 1st following a spin-up procedure needed to generate stable initial conditions (Supporting Information). Four years of further spin-up are excluded from each simulation due to an extended period of stratospheric spin-up in our simulations (Fig. S1 in Supporting Information). NATLx8 and NATLx4 simulations are extended to February 28th of model year 35, accumulating climate statistics over a total of 30 years per simulation. NE30 simulations are extended to February 28th of model year 55, accumulating climate statistics over a total of 50 years per simulation.

In addition to the reference simulations (referred to as REF throughout the rest of the text), we run two SST anomaly experiments for each grid. In the first, we increase the SST gradient over the longitudes 42-72°W in the Gulf Stream region, with SST anomalies linearly varying from 2°C at 38°N to $-2$°C at 44°N (Fig. 2a; referred to as GRAD throughout the rest of the text). In the second, SSTs are raised by 2°C everywhere within the Gulf Stream box (42-72°W, 38-44°N) (Fig. 2b; referred to as WARM throughout the rest of the text). In both cases, the SST anomalies are imposed in all seasons on top of the seasonally varying climatology described in the previous paragraph. The spatial ex-

**SST Forcing (Gradient Anomaly)**　　**SST Forcing (Warm Anomaly)**
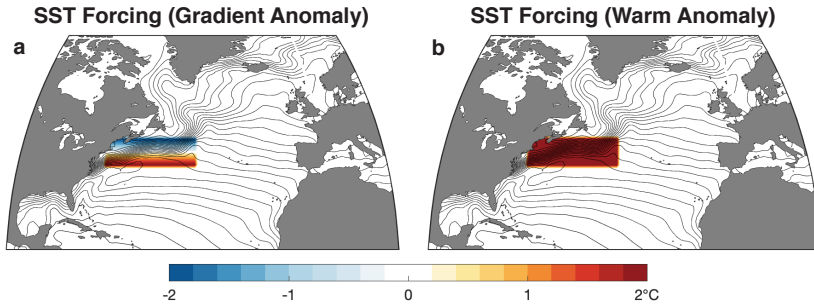


**Figure 2.** SST anomalies (shading) imposed in all months in the two idealized experiments: (a) The SST gradient anomaly experiment (GRAD); (b) the warm SST anomaly experiment (WARM). The DJF-mean SST climatology is shown in contours, with a contour interval of $1°C$.

tent of the imposed SST anomalies was chosen based on the large SST variance observed in this region (S. M. Wills et al., 2016).

The motivation for GRAD was to increase the SST gradient across the Gulf Stream. However, when we found that the results did not fit with our expectations for increased baroclinicity, we ran the WARM experiments to test whether the simulated response resulted from the increase in SST gradient or simply from the warming of SSTs in the southern part of the Gulf Stream region. Our results will show that for the NATLx8 and NATLx4 grids the WARM simulations produce surprisingly similar results to those in the GRAD experiments, suggesting that the warm SSTs in the southern part of the Gulf Stream region are the most important aspect of the imposed SST anomalies. Many other studies have used a smoothing of SSTs to reduce the SST gradient across the Gulf Stream (Nakamura et al., 2008; Kuwano-Yoshida et al., 2010; Parfitt et al., 2016; O'Reilly et al., 2016; O'Reilly et al., 2017; Sheldon et al., 2017; Vannière et al., 2017; Tsopouridis et al., 2021) without introducing abrupt SST jumps, such as occur at $38°N$ and $44°N$ in our simulations. In hindsight, we believe that this type of SST anomaly experiment may be easier to interpret than the ones used here. Nevertheless, the results of our idealized SST anomaly experiments (see Section 3) already provide substantial insight into how the atmospheric response to midlatitude SSTs varies with resolution.

Output is saved at monthly, daily, and 6-hourly temporal resolution. All output is conservatively remapped to a common $1.25°$ longitude $\times$ $0.94°$ latitude grid (referred to as f09) for plotting; the f09 grid has a grid spacing of 100-110 km (i.e., comparable to NE30) in the midlatitudes. In Section 3.5, we also utilize conservative remapping to a $2.5°$ longitude $\times$ $1.9°$ latitude grid (referred to as f19) to separate between large-scale and mesoscale anomalies. Unless otherwise indicated, 3D output is linearly interpolated from the model's hybrid coordinates to pressure coordinates (with 31 pressure levels) for plotting.

Our NATLx8 simulations exhibit large excursions in the global-mean stratospheric temperature, both at the beginning of the simulation and following model stability problems in model-years 10 and 11 of NATLx8-WARM and NATLx8-REF, respectively (Supporting Information Fig. S1a). There are corresponding anomalies in the stratospheric polar vortex strength, which stand out more from the background variability more in summer than in winter (Supporting Information Fig. S1). These excursions appear to be caused by reductions in the dynamics timestep that were made to keep the model stable during spin-up and for 1 to 2 days during the aforementioned model stability problems, but they persist for several years after the timestep has been returned to its default value. Because the stratospheric anomalies in the first 4 years affect all NATLx8 simulations,

we discard these years as spinup from the rest of our analysis. Only NATLx8-WARM is affected by large stratospheric anomalies in years 10-16, so in this case we simply test the sensitivity of our key result to the exclusion of the 6 affected DJFs, finding that it is unaffected by the exclusion of this period (Supporting Information Fig. S2). We there-fore show averages that include this period in all figures in the main text. More infor-mation about these stratospheric excursions is provided in the Supporting Information.

## 3  Results

Motivated by the potential implications for seasonal-to-decadal predictability, we focus our analysis on the response to the imposed SST anomalies, discussing aspects of how the climatology changes with resolution when it is relevant. The NAO in December-January-February (DJF) is a particularly important target for predictions, and as we will show, it has a large response to the SST forcing in the NATLx8 and NATLx4 simula-tions that is weaker or absent in the NE30 simulations. We therefore focus our analy-sis on DJF (See Supporting Information Fig. S3 for a look at the NAO response in other seasons). We note that in contrast to DJF, SON shows a larger NAO response in NE30 than in the higher resolution simulations, but we leave further investigation of this anomaly for future work.

### 3.1  Large-Scale Circulation Response

To visualize the large-scale circulation response to North Atlantic SST forcing in winter (DJF), we first show the DJF sea-level pressure response (Fig. 3). In the high-est resolution (14-km) NATLx8 simulations, there is a large East-Atlantic-intensified NAO-like response to the SST anomalies in both the GRAD and WARM experiments. It in-cludes a large ($\sim$ 4 hPa) negative SLP anomaly centered in the Norwegian Sea and a weaker positive SLP anomaly with lobes over the Gulf Stream and Mediterranean. The SLP response to the warm SST anomaly (WARM) has a similar spatial pattern in the (111-km) NE30 simulations but is weaker in magnitude, especially in the Norwegian Sea. The response to the SST gradient anomaly (GRAD) is very weak in NE30, with a com-pletely different spatial pattern. If the NATLx8 responses can be thought of as the cor-rect response, then the SLP responses in the (28-km) NATLx4 simulations represent an improvement compared to NE30, but they show a different spatial pattern with much weaker negative anomalies in the Norwegian Sea and stronger positive anomalies over Western Europe. Note that the magnitudes of the SLP responses and other key circu-lation responses will be tabulated in Section 4.

To test the significance of these responses with respect to internal variability, we recompute differences from bootstrapped resampling of the three simulations (REF, GRAD, and WARM) at each resolution. Differences are computed between averages of $n' = n(1-a)/(1+a)$ resampled years, where $n$ is the number of years used to compute the response (i.e., 30 for NATLx8/NATLx4 and 50 for NE30) and $a$ is the absolute value of the zonal-mean 1-year autocorrelation of seasonal averages at each latitude. The autocorrelation factor corrects for the presence of autocorrelation in the original averages that is not present in the resampled averages (Trenberth, 1984). We find that a large region of negative SLP anomalies in the Norwegian Seas is significant (0.1 significance level based on two-tailed t-test; stippling in Fig. 3) in both NATLx8 simulations. The positive SLP anomaly in the Mediterranean is also significant in NATLx8-GRAD. NATLx4 shows similar regions of significant SLP anomalies (Western Europe and Scandinavia/western Russia) in both simulations. NE30-WARM shows only small regions of significant SLP anomalies over the North Atlantic and Europe, even with its longer 50-year averages, however, both NE30 simulations show a large region of weakly positive but significant SLP anomalies over the southeast U.S. These results are similar if 30-year averages are used instead of 50-year averages for NE30 (Fig. S4 in Supporting Information).
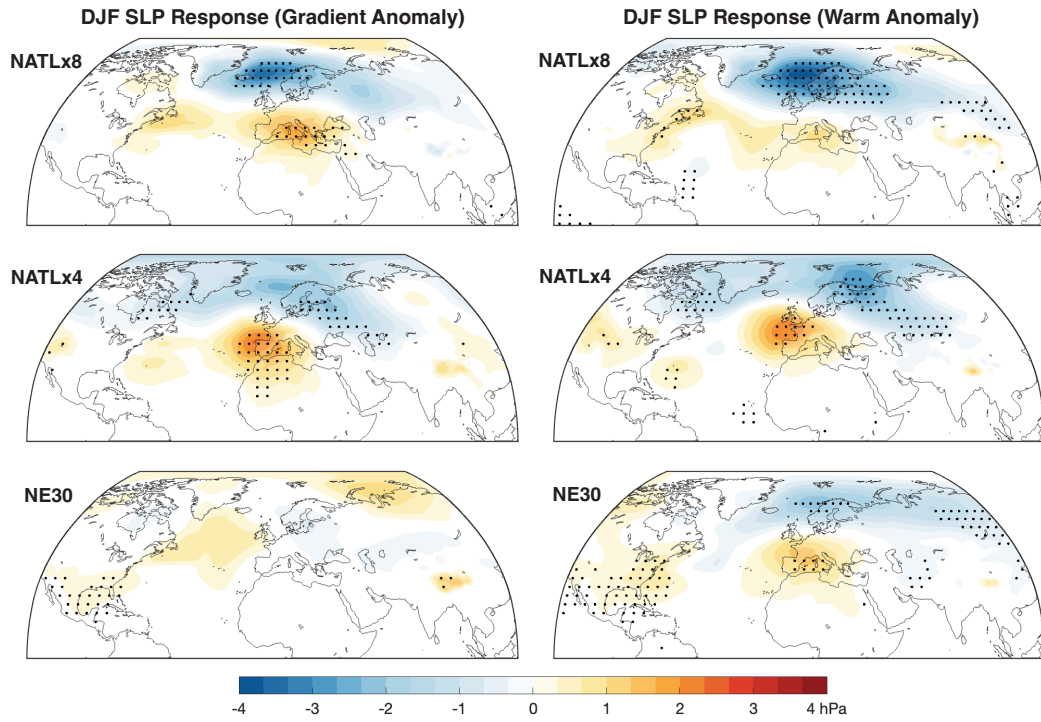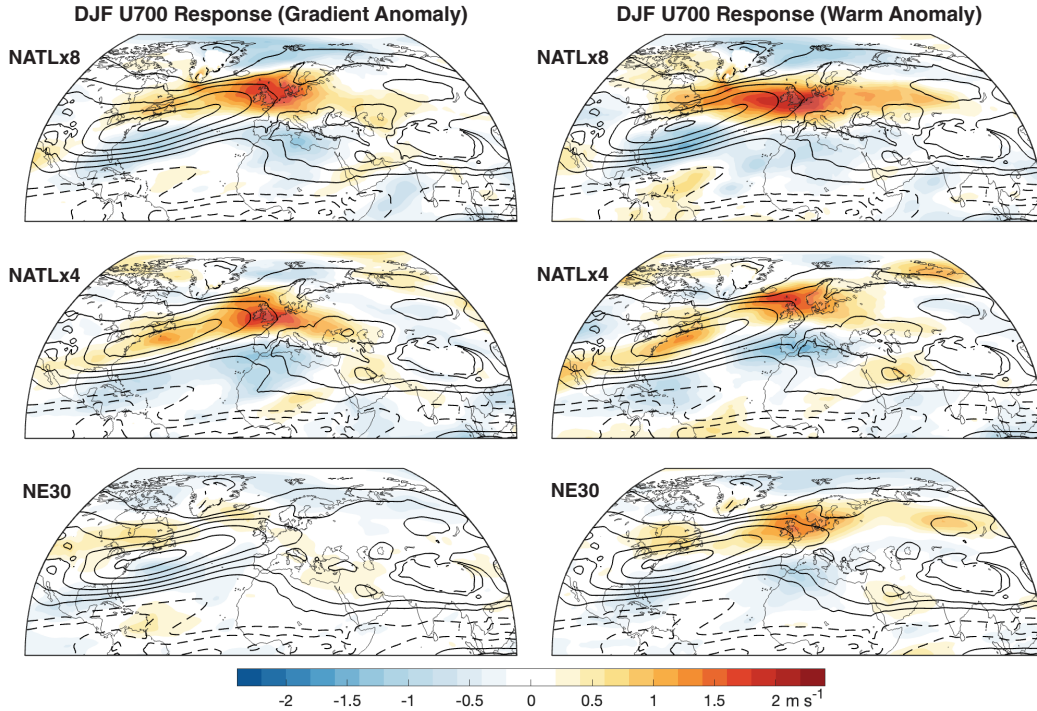
**Figure 3.** DJF Sea-level pressure (SLP) response to an SST gradient anomaly (GRAD-REF; left) and a warm SST anomaly (WARM-REF; right) in the Gulf Stream, in 3 different configurations of CAM-SE: (top) NATLx8, with 14-km resolution in the North Atlantic, (middle) NATLx4, with 28-km resolution in the North Atlantic, and (bottom) NE30, with global 111-km resolution. Anomalies are the difference of 30-year averages in NATL and 50-year averages in NE30. Stippling denotes anomalies that are significant (0.1 significance level) compared to internal variability, diagnosed by bootstrap sampling an equivalent number of independent seasonal averages, accounting for the autocorrelation between seasonal averages as described in the text, and then applying a two-tailed t-test.
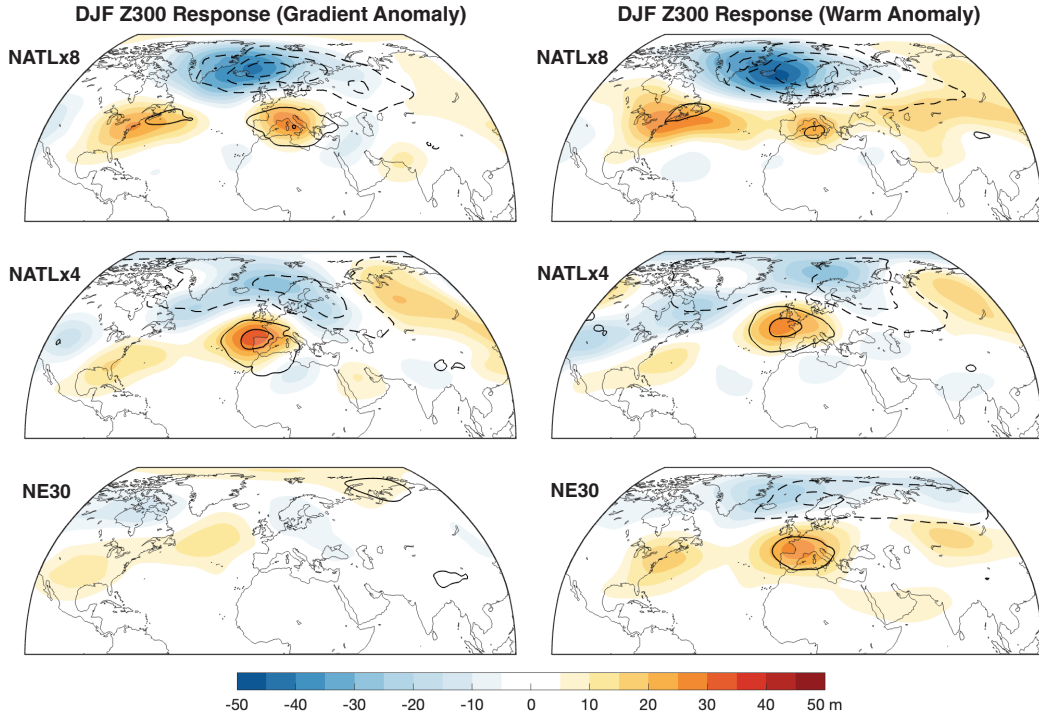
**Figure 4.** DJF 300 hPa geopotential height (Z300) response (shading) to an SST gradient anomaly (GRAD-REF; left) and a warm SST anomaly (WARM-REF; right) in the Gulf Stream, in 3 different configurations of CAM-SE: NATLx8, with 14-km resolution in the North Atlantic, NATLx4, with 28-km resolution in the North Atlantic, and NE30, with global 111-km resolution. Anomalies are the difference of 30-year averages in NATL and 50-year averages in NE30. Black contours show the DJF SLP response, as shown in Fig. 3, with a contour interval of 1 hPa; negative anomalies are dashed and the zero contour is omitted.

Notably, the similar spatial patterns of SLP response between NE30-WARM and NATLx8-WARM, but with much larger magnitudes in NATLx8-WARM, is exactly what we should see for this to help alleviate the signal-to-noise paradox (Eade et al., 2014; Scaife & Smith, 2018; D. M. Smith et al., 2020). The signal-to-noise paradox is based on the finding that models predict the observations well for some quantities (e.g., the NAO), but with a reduced amplitude of anomalies, such that the scaled-up ensemble mean has more skill in predicting the observations than would be expected from the skill in predicting individual ensemble members. Our results suggest that increasing the resolution of atmospheric models to better resolve frontal processes could increase the magnitude of responses to SST anomalies. In modeling configurations that skillfully predict SSTs, the increase in resolution would also increase the magnitude of predictable SLP anomalies, reducing the signal-to-noise paradox. Our results indicate that $1/4°$ spatial resolution may not be enough to recover the full strength of the atmospheric response to midlatitude SST anomalies, and we have no way of knowing whether the response has converged at $1/8°$ spatial resolution. The implications for the signal-to-noise paradox will be discussed further in Section 4.

The difference in circulation response between NATLx8 and NATLx4 is even more apparent in the upper troposphere, as seen in the 300-hPa geopotential height (Z300) responses (Fig. 4). The NATLx8 Z300 responses show similar spatial patterns to the SLP response, with a westward phase shift indicating an upward propagating stationary wave.

**Figure 5.** DJF 700 hPa zonal wind (U700) response (shading) to an SST gradient anomaly (GRAD-REF; left) and a warm SST anomaly (WARM-REF; right) in the Gulf Stream, in 3 different configurations of CAM-SE: NATLx8, with 14-km resolution in the North Atlantic, NATLx4, with 28-km resolution in the North Atlantic, and NE30, with global 111-km resolution. Black contours show the climatology in the reference simulation (REF) with a contour interval of 3 m s$^{-1}$; negative anomalies are dashed and the zero contour is omitted). Anomalies are the difference of 30-year averages in NATL and 50-year averages in NE30.

The NATLx4 Z300 response shows weaker anomalies with no phase shift compared to the SLP response, indicating a stationary wave that is decaying with height. In NE30, there are strong westward shifted anomalies in the WARM experiment but weak anomalies with no phase shift in the GRAD experiment.

Next, motivated by the finding that models have much weaker decadal variability in the zonal-wind at 700 hPa (U700) than is found in reanalysis (Simpson et al., 2018), we investigate the U700 response to SST anomalies at each resolution (Fig. 5). All simulations except NE30-GRAD show a stronger eastward extension of the climatological winds into the UK and Scandinavia in response to the SST anomalies. This response is strongest in NATLx8-WARM, then has similar magnitudes in NATLx8-GRAD, NATLx4-WARM, and NATLx4-GRAD, but with the largest area of strong anomalies in NATLx8-GRAD. NE30-WARM shows a spatially similar but weaker response in this region. These results indicate that multi-decadal variance in U700 could increase at higher resolution in cases where SSTs vary on multi-decadal timescales. The U700 response varies more with resolution in the Gulf Stream SST forcing region: NATLx8 and NE30 show a poleward wind shift in this region that is stronger in NATLx8 than in NE30, however, NATLx4 instead shows an intensification of the zonal winds near their climatological maximum. These differences don't appear to stem from differences in the climatological winds, which are similar across the different resolutions (black contours in Fig. 5).
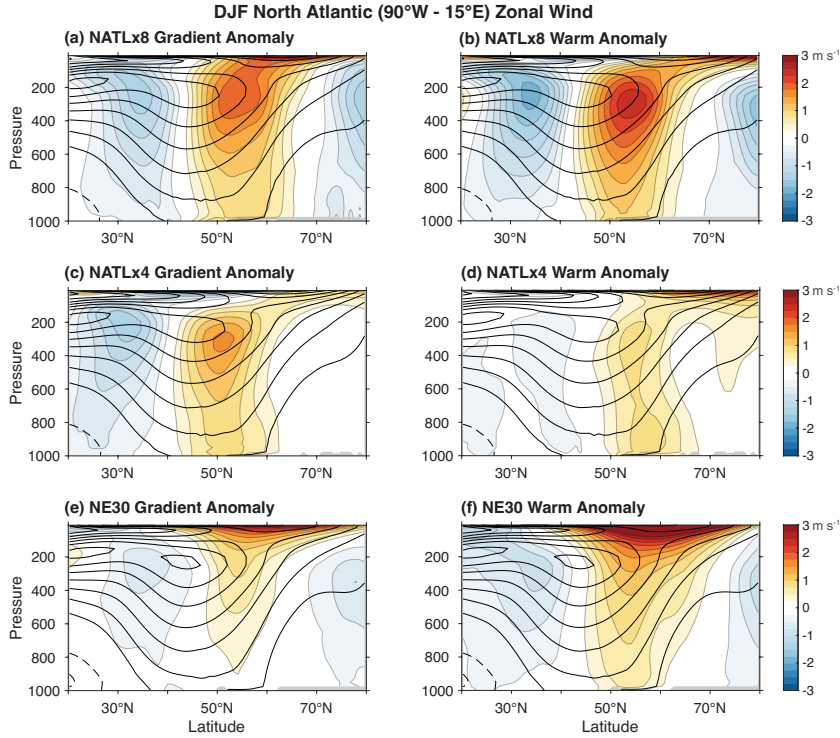
**Figure 6.** Same as Fig. 5, but for the DJF zonal-mean zonal winds over the Atlantic sector (90°W-15°E) as a function of latitude and pressure. The contour interval for the climatology is 4 m s$^{-1}$; negative anomalies are dashed and the zero contour is omitted.

Due to the increasing amplitude of anomalies with height in NATLx8 and the cancellation of anomalies between the eastern and western North Atlantic in NATLx4, the zonal-mean zonal winds over the Atlantic sector show much larger anomalies in response to SST forcing in NATLx8 than in any of the the lower resolution simulations (Fig. 6). All simulations show a poleward shift of the North Atlantic jet, but with different magnitudes and vertical structures. There are some minor differences in the climatology of the North Atlantic zonal winds with resolution, most notably stronger maximum winds in the eddy-driven jet in NE30 compared to NATLx4 and NATLx8 and stronger winds in the "neck region" (i.e., at ∼ 100 hPa between the eddy-driven jet and the stratospheric polar vortex) in NATLx4 compared to NE30 and NATLx8 (black contours in Fig. 6).

### 3.2 Projection onto modes of internal variability

To characterize how the large-scale circulation response to SST anomalies projects onto the dominant modes of variability, we compute the EOFs of pentadal (5-day-mean) SLP in the North Atlantic (90°W-40°E, 15-80°N). We compute the EOFs using 29-years (due to missing daily data in one year) of DJF data from each of the 9 simulations to obtain a common set of EOFs that explain the variability across all simulations (the EOFs computed separately for each resolution are shown in Supporting Information Fig. S5). The leading EOF (24% variance explained) represents the NAO (Fig. 7a). The second EOF (18% variance explained) shows a low pressure anomaly centered in the North Sea and is similar to the East Atlantic pattern (Fig. 7b). The magnitude of both patterns is between 12 and 13 hPa, already giving a sense that the ∼4 hPa time-mean anomalies in response to SST anomalies are not small, even compared to synoptic (pentadal) variability.
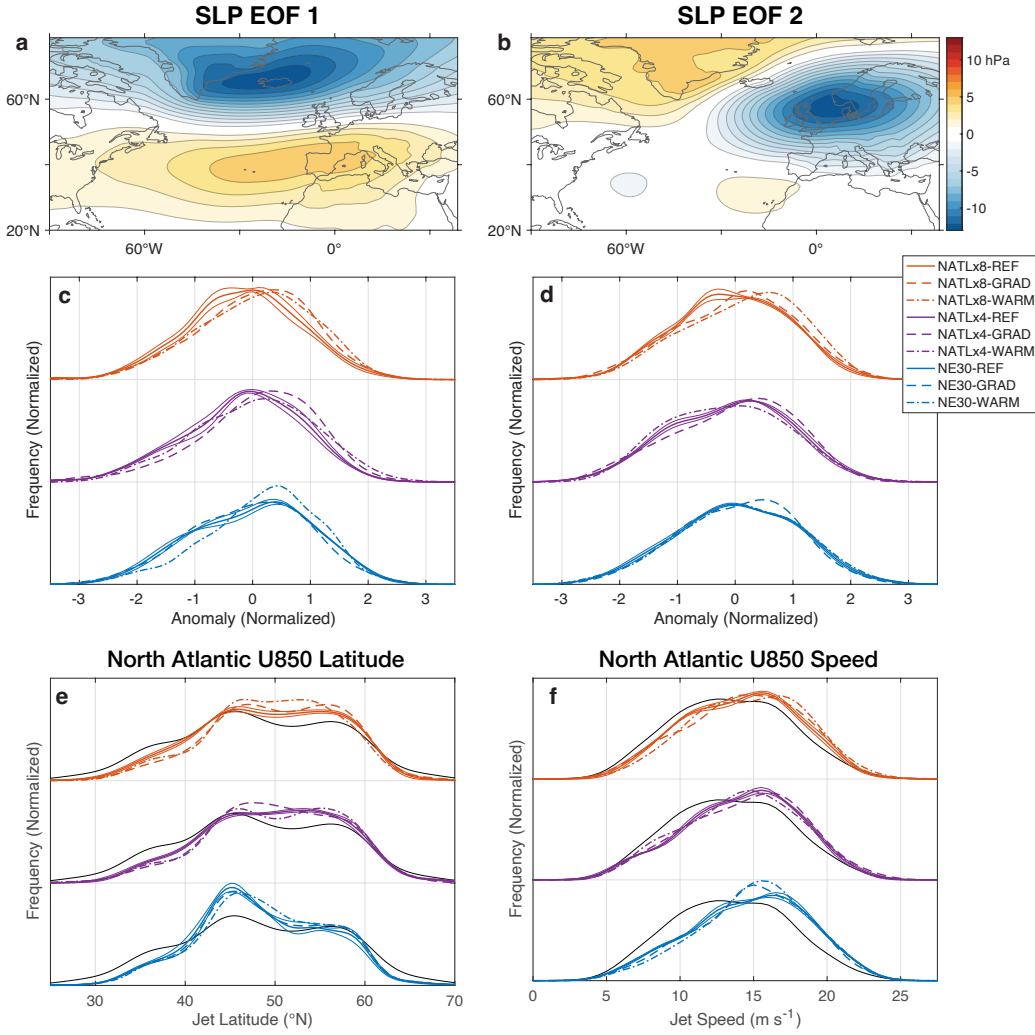
**Figure 7.** (a)-(d) Empirical orthogonal functions (EOFs) of pentadal-mean sea-level pressure (SLP) anomalies in DJF across all 9 simulations, where anomalies are with respect to the average climatology over all 9 simulations and thus include climatological differences. (a) EOF 1, (b) EOF2, (c) probability distribution of principal component 1 in each simulation, (d) probability distribution of principal component 2 in each simulation. The EOFs shown in (a) and (b) are equivalent to the anomaly when the associated principal component is equal to 1. (e) Normalized probability distributions of the pentadal-mean latitude of maximum North Atlantic jet speed during DJF in each simulation and (f) the same for the jet speed at this maximum. The North Atlantic jet is defined as the zonal-mean of the zonal wind at 850 hPa over 0-60°W. In (e) and (f), the black lines show the same analysis applied to ERA5 over 1979-2022. Probability distributions are estimated with kernel density estimation (Botev et al., 2010). Sampling uncertainty in the probability distributions is estimated by splitting each simulation into three segments and dividing the variance in the probability distribution across the segments by 3; the resulting 1-standard-deviation spread is shown for the REF simulations as thin solid lines.

The distribution of principal components are shown separately for each simulation in Figs. 7c and 7d. In NATLx8, there is a positive shift in the mean of 0.19 (0.21) standard deviations in EOF 1 and of 0.07 (0.20) standard deviations in EOF2 in response to SST anomalies, for GRAD (WARM) compared to REF. These are responses compared to the pentadal variability, and when compared to interannual variability they instead correspond to shifts in the mean of 0.41 (0.44) standard deviations in EOF 1 and of 0.21 (0.61) standard deviations in EOF2, for GRAD (WARM) compared to REF. NATLx4-GRAD (NATLx4-WARM) show a similar positive shift in the mean of EOF1 of 0.52 (0.42) interannual standard deviations but a smaller shift in the mean of EOF 2 of 0.15 (-0.15) interannual standard deviations. In NE30-WARM, the probability of negative EOF 1 values is reduced in favor of an increase in the probability of weakly positive EOF 1 values, near the peak of the distribution, corresponding to a shift in the mean of 0.35 interannual standard deviations, but it has no meaningful change in the distribution for EOF 2 (a mean shift of 0.14 interannual standard deviations). NE30-GRAD does not show much of a shift in either EOF, with mean shifts of -0.12 and 0.13 interannual standard deviations in EOFs 1 and 2, respectively. Overall, this analysis shows that the SST anomalies both lead to large ($\sim$0.5 interannual-standard-deviation) anomalies in the leading mode of SLP variability (i.e., the NAO) in NATLx8 and NATLx4 that are weaker or absent in NE30, and that NATLx8-WARM shows a much larger response in EOF 2 than any of the other simulations.

North Atlantic circulation variability has also been characterized by the latitude of the jet maximum, which has been shown to exhibit regime-like behavior not apparent from the EOFs of SLP (Woollings et al., 2010; White et al., 2019; Strommen et al., 2019; Strommen, 2020; Dorrington et al., 2022). Following Strommen (2020), we compute the North Atlantic jet latitude as the latitude of the maximum in the zonal-mean 850-hPa zonal winds in the North Atlantic (0-60°W). We use pentadal averages in place of the 9-day running mean used in Strommen (2020). NATLx8 has the most realistic structure of the jet latitude probability distribution compared to ERA5 Reanalysis (Hersbach et al., 2020) (Fig. 7e), but all 3 resolutions of CAM6-SE show too little occurrence of the southernmost jet latitude peak at 35°N. The 45°N jet latitude peak is too strong in NE30, whereas it is more realistic in NATLx4 and NATLx8. Both NATLx4 and NATLx8 have a relatively larger probability (compared to NE30 and ERA5) of jets occurring at the northern peak, the presence of which has been linked to Greenland topography and Greenland tip-jet events (White et al., 2019). Overall, there is some indication that the regime-like behavior of jet latitude increases with resolution (cf. Strommen, 2020), which is apparent in the less peaked probability distributions in NATLx4 and NATLx8 compared to NE30. In terms of jet speed, NATLx8 is again most realistic compared to ERA5 reanalysis (Fig. 7f).

In response to both SST anomalies, NATLx8 and NATLx4 show increases in the probability of jets at the midlatitude and northern peaks at the expense of jets at the southern peak (Fig. 7e) and a slight shift towards stronger jet speeds (Fig. 7f). In contrast, NE30-WARM (and to a lesser extent NE30-GRAD) shows a more peaked jet speed distribution, a poleward shift of the midlatitude peak, an increase in the probability of jets at the northern peak, and no change in the probability of jets at the southern peak. Overall, this shows that the circulation response to SST anomalies is more complex than a simple mean shift in circulation and it is associated with a shift in probability of occurrence of the underlying circulation regimes.

### 3.3 Air-Sea Interactions and Cross-Front Circulation Response

As a first step in analyzing the mechanisms for the large NAO-like response to SST anomalies and its dependence on resolution, we investigate the air-sea interactions and the cross-front circulation response in the SST forcing region.
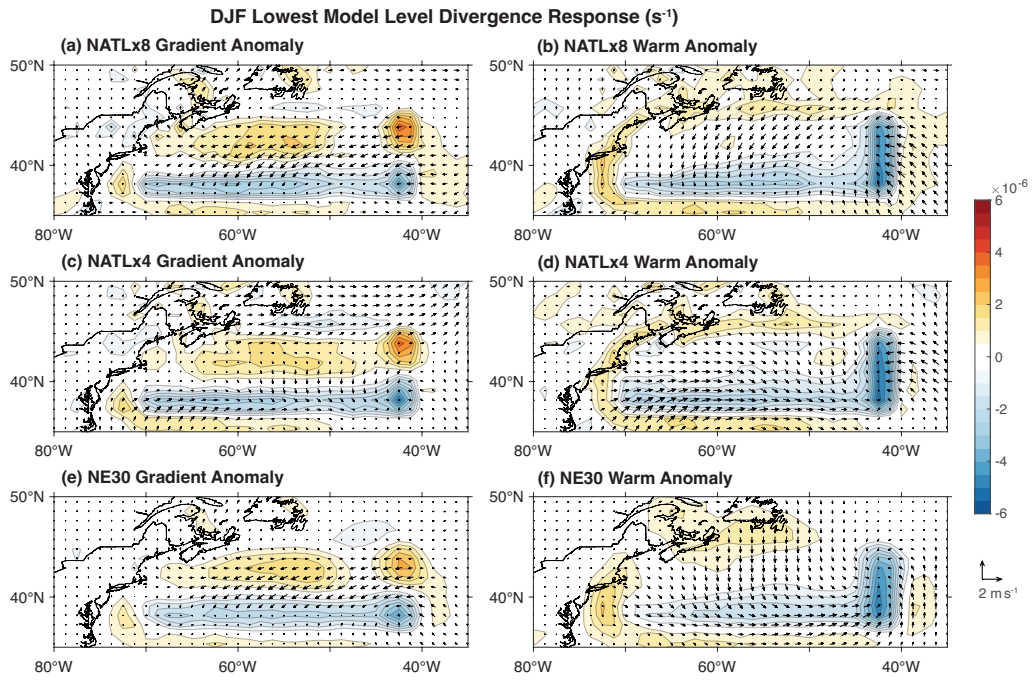
**Figure 8.** DJF near-surface (lowest model level) zonal and meridional wind (arrows) and divergence (shading) response to an SST gradient anomaly (GRAD-REF; left) and a warm SST anomaly (WARM-REF; right) in the Gulf Stream, in 3 different configurations of CAM-SE: NATLx8, with 14-km resolution in the North Atlantic, NATLx4, with 28-km resolution in the North Atlantic, and NE30, with global 111-km resolution. Anomalies are the difference of 30-year averages in NATL and 50-year averages in NE30.
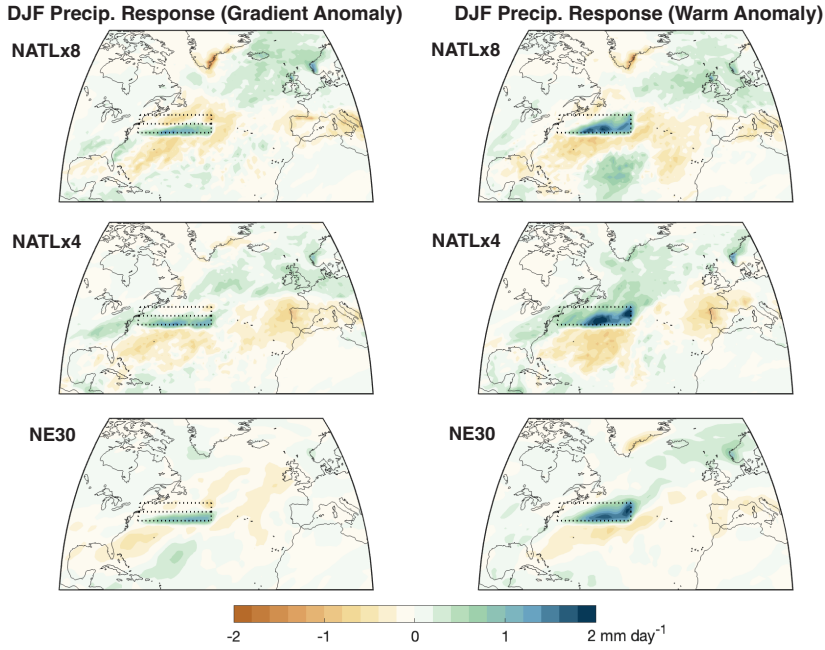
**Figure 9.** DJF precipitation response to an SST gradient anomaly (GRAD-REF; left) and a warm SST anomaly (WARM-REF; right) in the Gulf Stream, in 3 different configurations of CAM-SE: (top) NATLx8, with 14-km resolution in the North Atlantic, (middle) NATLx4, with 28-km resolution in the North Atlantic, and (bottom) NE30, with global 111-km resolution. Anomalies are the difference of 30-year averages in NATL and 50-year averages in NE30.

Much of the literature on how ocean resolution impacts the atmospheric response to SST anomalies has focused on the near-surface wind divergence (e.g., Small et al., 2014), because it is related to the Laplacian of SST through the pressure adjustment mechanism (Lindzen & Nigam, 1987; Minobe et al., 2008) and to the downwind SST gradient by the vertical mixing mechanism (Hayes et al., 1989; Chelton et al., 2001), and because both the Laplacian of SST and the downwind SST gradient are sensitive to the ocean resolution. However, we find that the near-surface wind divergence response is very similar across different atmospheric resolutions (despite differences in the response of the individual near-surface wind components; Fig. 8). This suggests that differences in near-surface divergence response are not the reason for the differences in large-scale circulation response. This is perhaps not surprising considering the strong relationship between near-surface divergence and SST, which is kept the same as the atmospheric resolution is varied. Indeed, the spatial pattern of near-surface divergence matches well with the downwind SST gradient (leading to large anomalies on the eastern boundary of the forcing region) and the Laplacian of SST (leading to large anomalies on the southern boundary of the forcing region), as expected from these boundary layer theoretical considerations.

Precipitation anomalies somewhat resemble the near-surface convergence anomalies (Fig. 9), with anomalies over the forcing region of 1-2 mm/day, more than 20% of the climatological precipitation in this region. Like the near-surface convergence, they do not show large differences across the different resolutions. It therefore does not appear that differences in the time-mean precipitation and latent heating are responsible for the difference in large-scale circulation response. For example, the experiment with the largest precipitation response (NATLx4-WARM) does not have the largest large-scale circulation response (cf. Figs. 3-6). Note, however that the precipitation anomalies over
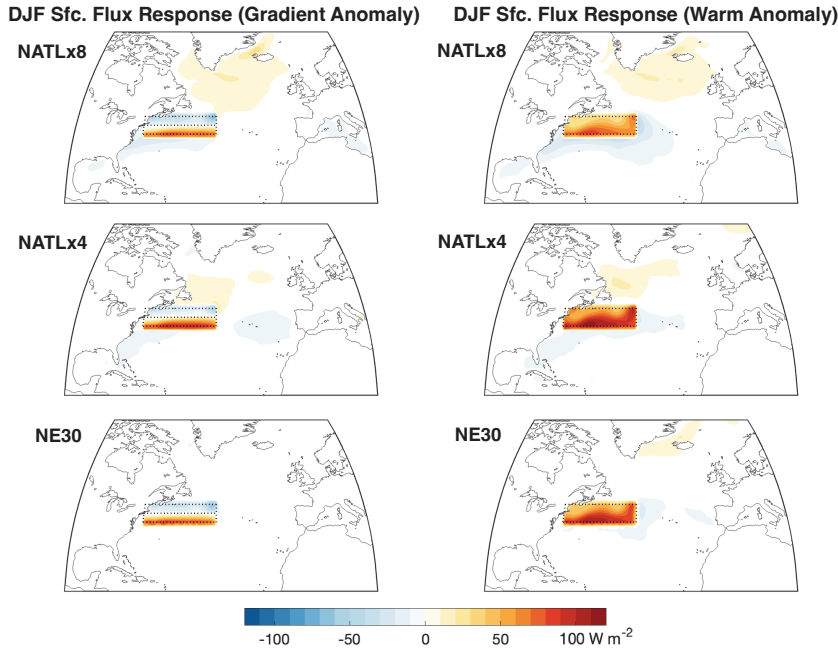
**Figure 10.** Same as Fig. 9, but for DJF surface turbulent (latent + sensible) heat flux.

471 the SST forcing are bounded by dry anomalies to the north in NATLx8, whereas they
472 are continuous with enhanced precipitation anomalies to the north in NATLx4. This is
473 a qualitative indication that precipitation occurs through local convective process in NATLx8
474 versus as part of the larger-scale warm conveyer belt in NATLx4, as will be discussed
475 in Section 3.5. Note also that while the time-mean precipitation is similar across reso-
476 lutions, the spatial contrast in precipitation and latent heating between different parts
477 of cyclones could increase at higher resolution (Schemm, 2023), potentially causing more
478 rapid cyclone growth. Downstream of the forcing region, the non-local responses (e.g.,
479 in the subpolar North Atlantic and Western Europe) are larger in the NATLx4 and NATLx8
480 simulations as a result of the larger large-scale circulation responses, with anomalies in
481 the eastern North Atlantic and Europe of up to 10-20% of the climatological DJF pre-
482 cipitation in these regions.

483    Given the use of specified-SST experiments, a natural question arises of whether
484 the SST anomalies correspond to comparable surface turbulent (latent + sensible) heat-
485 flux anomalies as the atmospheric resolution is varied. Similar to what was found for near-
486 surface divergence and precipitation, the anomalies in turbulent heat fluxes are differ-
487 ent between the GRAD and WARM experiments, but the differences with resolution are
488 relatively small (Fig. 10). There is some variation in the magnitude of surface fluxes with
489 resolution, especially for the WARM experiment, with the largest values in NATLx4 and
490 the smallest in NATLx8. This means that NATLx8 gives the largest large-scale circu-
491 lation response despite having the smallest surface heat-flux anomalies. The surface flux
492 differences are related to differences in the adjustment of near-surface air temperature,
493 with near-surface air temperature anomalies being largest in NATLx8 and smallest in
494 NATLx4 (not shown).

495    The differences in air-temperature adjustment over the SST anomalies are also ev-
496 ident further into the troposphere; NATLx8-GRAD, NATLx8-WARM, and (to a lesser
497 extent) NE30-WARM all show deep warm anomalies over the forcing region (42-72°W;
498 Fig. 11). The differences across the simulations in the magnitude of potential temper-
499 ature response over the forcing region mirror the differences in the magnitude of the up-

per tropospheric circulation response (cf. Figs. 4 and 6), a simple consequence of thermal wind balance. Explaining the differences in the free-tropospheric potential temperature response in the forcing region is therefore key to understanding the differences in the large-scale circulation response between simulations. The horizontal spatial structure of these deep temperature anomalies can most clearly be seen in Z300 (Fig. 4), which is related to the vertically averaged temperature anomaly below 300 hPa. The potential temperature responses over the forcing region look different in both NATLx4 experiments compared to those in the other simulations, with a warm anomaly to the south of the forcing region and a cold anomaly to the north (Fig. 11; cf. Fig. 4), consistent with the increase in wind speed at the jet maximum that was seen in Fig. 5.

Fig. 11 also shows anomalies in the time-mean ageostrophic meridional and vertical winds over the Gulf Stream SST front. The time-mean upward motion is not very different between the different simulations; all experiments show anomalous upward motion extending to between 400 and 500 hPa. However, there are large differences in the ageostrophic meridional winds. While much of the ageostrophic meridional wind anomalies over the Gulf Stream SST anomalies in NATLx8 appear to make up a closed meridional circulation, with ascent near 38°N and descent near 45°N, the ascending air anomalies instead turn equatorward in NATLx4 and (to a lesser extent) NE30, similar to what was found in Smirnov et al. (2015). Thus only the NATLx8 experiments (and to a lesser extent NE30-WARM) have poleward ageostrophic winds in the upper troposphere, which can provide an important source of zonal momentum.

### 3.4 Thermodynamic Analysis

To gain insight into the maintenance of the deep temperature anomalies in NATLx8-GRAD, NATLx8-WARM, and NE30-WARM, we analyze the thermodynamic equation for the mid-troposphere (300-800 hPa) over the forcing region (42-72°W; 38-44°N):
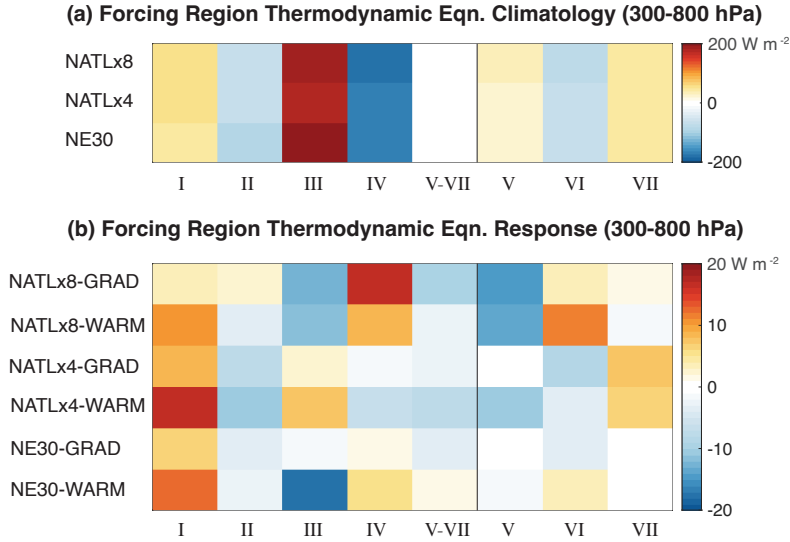
$$\underbrace{\overline{Q}}_{\text{I}} - \underbrace{(\overline{\omega}\partial_p\overline{T} - \kappa\frac{\overline{\omega}\overline{T}}{p})}_{\text{II}} - \underbrace{\overline{v}\nabla_y\overline{T}}_{\text{III}} - \underbrace{\overline{u}\nabla_x\overline{T}}_{\text{IV}} - \underbrace{\nabla_x \cdot \overline{u'T'}}_{\text{V}} - \underbrace{\nabla_y \cdot \overline{v'T'}}_{\text{VI}} - \underbrace{(\partial_p(\overline{\omega'T'}) - \kappa\frac{\overline{\omega'T'}}{p})}_{\text{VII}} = 0.$$

(1)

Here, overbars denote monthly averages, primes denote deviations from the monthly mean, $\nabla_x$ and $\nabla_y$ are the zonal and meridional components of the nabla operator on a sphere, $Q$ is the total diabatic heating (including latent heating, radiation, and parameterized turbulent diffusion), $\kappa = R/c_p = 2/7$ is the ratio of the specific gas constant and specific heat capacity of dry air, and all other variables follow standard meteorological conventions. Over the Gulf Stream, the dominant balance is between meridional warm air advection (Term III) and zonal advection of cold air off the North American continent (Term IV) (Fig. 12a). There is also time-mean upward motion (Term II) and diabatic (latent) heating (Term I). The total effect of transient-eddy heat-flux convergence (Terms V-VII) is small due to cancellation between heating by zonal and vertical eddy heat transport and cooling from meridional eddy heat transport. These balances stay roughly the same as the resolution is changed.

The response of the terms in the thermodynamic equation (in the mid troposphere) to the imposed SST anomalies shows more varied behavior across the different resolutions. All simulations show an increase in latent heating in response to the SST anomalies (Fig. 12b; Term I); this increase in latent heating is largest in the WARM experiments, owing to a partial compensation by negative anomalies in the northern part of the forcing domain in the GRAD experiments (not shown). While the latent heating anomalies are largest in the NATLx4 simulations, matching what was found for precipitation and surface fluxes (cf. Figs. 9 and 10), they are compensated in these simulations by larger negative anomalies in the vertical advection term (Fig. 12b; Term II). Rather than resulting from differences in time-mean ascent, which is similar across the resolutions (Fig. 11), these differences in Term II result from differences in stratification in the ascent re-

**DJF Forcing Longitudes $v_a$, $\omega$, and $\theta$ Response**
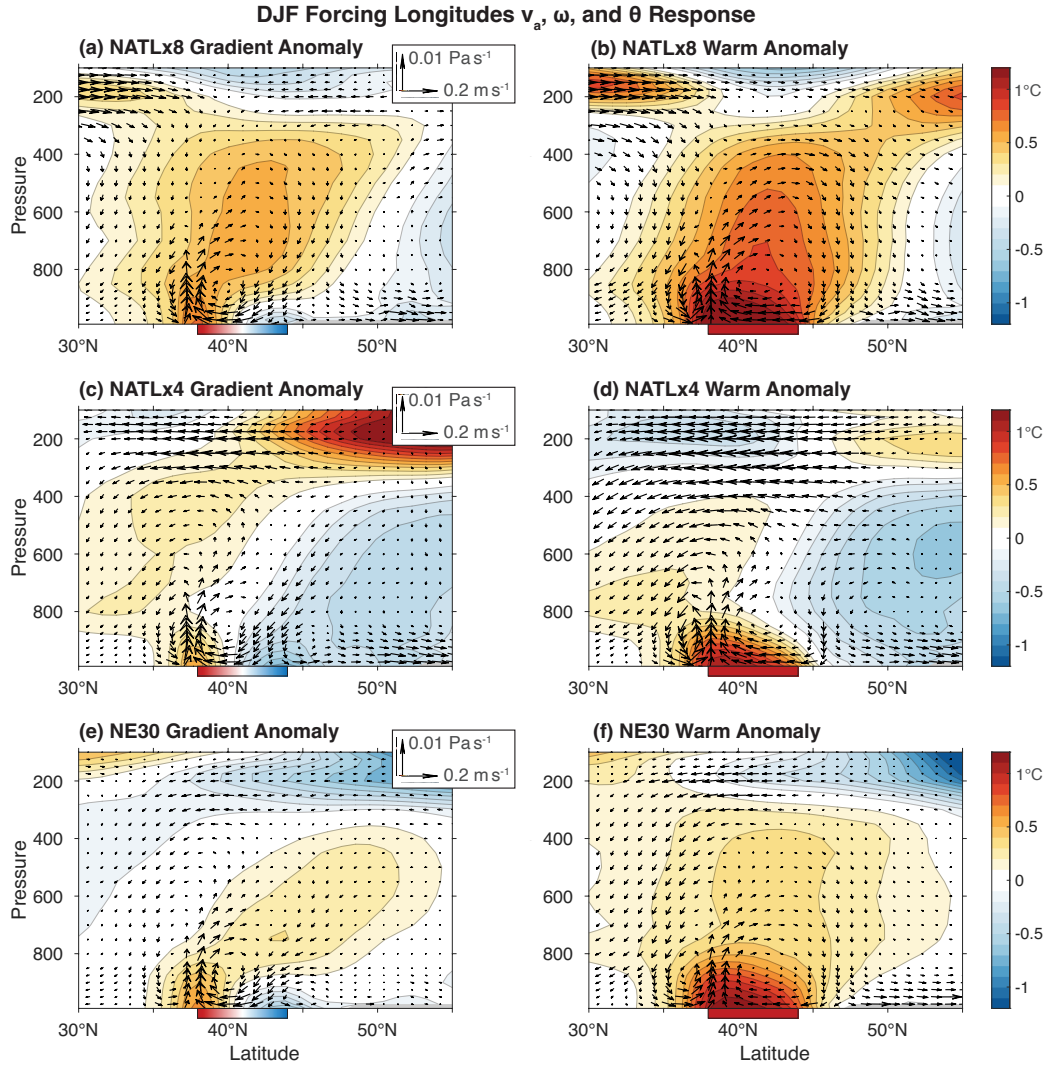
**Figure 11.** Average over the forcing longitudes (42-72°W) of the DJF potential temperature (shading) and ageostrophic meridional and vertical wind (arrows) response to an SST gradient anomaly (GRAD-REF; left) and a warm SST anomaly (WARM-REF; right) in the Gulf Stream, in 3 different configurations of CAM-SE: (top) NATLx8, with 14-km resolution in the North Atlantic, (middle) NATLx4, with 28-km resolution in the North Atlantic, and (bottom) NE30, with global 111-km resolution. Anomalies are the difference of 30-year averages in NATL and 50-year averages in NE30.

**(a) Forcing Region Thermodynamic Eqn. Climatology (300-800 hPa)**



**(b) Forcing Region Thermodynamic Eqn. Response (300-800 hPa)**



**Figure 12.** Average over the forcing longitudes (42-72°W) and latitudes (38-44°N) of (a) the DJF climatology (REF) of the terms in the thermodynamic equation (Eq. 1), including a column showing the sum of terms V-VII, and (b) responses of these terms to an SST gradient anomaly (GRAD-RED) and a warm SST anomaly (WARM-REF) in the Gulf Stream, in 3 different configurations of CAM-SE. Anomalies are the difference of 30-year averages in NATL and 50-year averages in NE30.

gion, which decreases in response to the SST anomalies in NATLx8, as well as from anomalous time-mean subsidence on the northern and southern edges of the forcing region, which is strongest in the NATLx8 SST anomaly experiments. This means that the effective forcing from vertical motions after accounting for the cancellation between adiabatic cooling and latent heating (Term I + Term II) is similar across different resolutions.

Despite broad similarities in the first two terms, the response in the horizontal advection terms (Eq. 1; Terms III and IV) are opposite between the simulations with deep temperature anomalies (NATLx8 and NE30-WARM) and those with free-tropospheric temperature gradient anomalies (NATLx4): NATLx4 shows a strengthening of the climatological meridional warm-air advection and zonal advection of cold air off the continent, whereas NATLx8 and NE30-WARM show a weakening of the climatology (Fig. 12b; Terms III and IV). The negative meridional advection anomalies (Term III) for NATLx8 and NE30-WARM result from a combination of northerly wind anomalies (not shown in Fig. 11 because they are geostrophic) and weakened meridional temperature gradient, whereas the positive anomalies in NATLx4 result primarily from the strengthened meridional temperature gradient (Fig. 13). The meridional temperature gradient response (Fig. 13) shows a poleward shift in NATLx8 and NE30-WARM but a strengthening near its maximum for NATLx4, as was seen for the U700 response (Fig. 5). Similarly, the changes in zonal advection (Term IV) in NATLx8 can be partially understood in terms of changes in horizontal temperature gradients, with a tropospheric warming over the U.S. eastern seaboard reducing the zonal temperature gradient in NATLx8 and NE30-WARM but a cooling over Atlantic Canada increasing the zonal temperature gradient in NATLx4 (Fig. 4). Interestingly, Famooss Paolini et al. (2022) also see switches in sign of the time-mean meridional and zonal advection terms between 100-km- and 50-km-resolution models, in agreement with the changes between NE30 and NATLx4; however, we see another switch in sign of these terms going from NATLx4 (28 km) to NATLx8 (14 km).
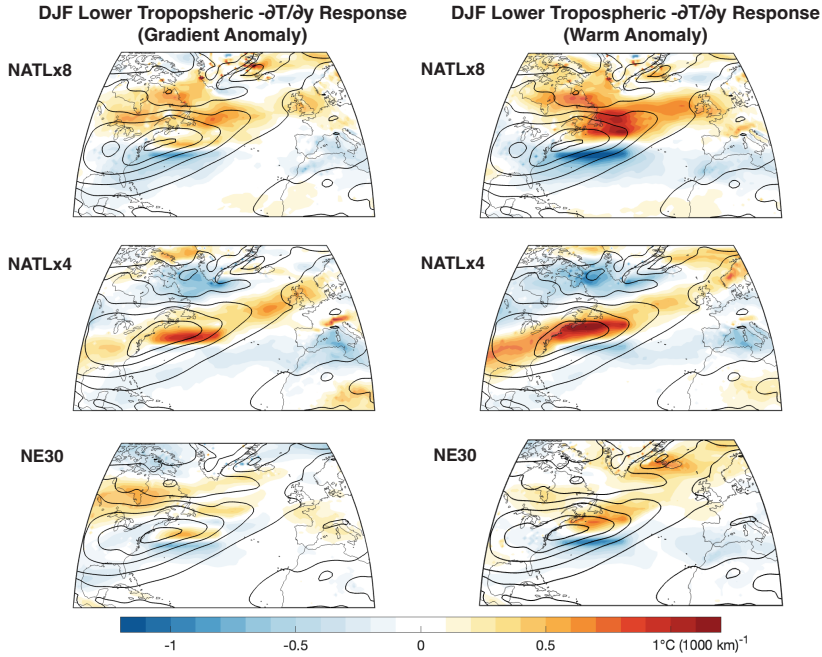
**Figure 13.** Same as Fig. 5, but for the DJF vertically averaged meridional temperature gradient below 500 hPa, with flipped sign such that a poleward decrease in temperature is positive. The contour interval for the climatology (which has been spatially smoothed with a $1.5°$ Gaussian filter) is $2°C$ $(1000$ km$)^{-1}$.

Thus far, our analysis of the thermodynamic equation has illustrated differences across resolutions in the response of the dominant terms, but it has not provided a definitive answer to what is driving the deeper warm anomalies in NATLx8 and NE30-WARM. This is in part inherent to any analysis of the thermodynamic equation, where individual terms influence but are also influenced by the distribution of temperature anomalies. However, there are only a few terms with anomalously positive tendencies in response to SST anomalies in NATLx8 than NATLx4, such that they could explain a larger free-tropospheric warming in NATLx8: vertical advection (Term II), zonal advection (Term IV), and meridional eddy heat-flux (EHF) convergence (Term VI). It has already been discussed how the zonal and vertical advection anomalies are a consequence of the deep temperature anomaly, which reduces the zonal temperature gradient and the lapse rate. Therefore, in the next section we turn our attention to the responses of meridional EHF and other transient-eddy heat fluxes to SST forcing and how they depend on resolution. The basic picture that emerges is that frontal processes move heat vertically in NATLx8, creating a deep warm temperature anomaly that reduces the meridional temperature gradient and thus the meridional EHF, the divergence of which would otherwise act to damp the temperature anomaly. In contrast, when eddies move heat vertically in NATLx4, they do so as part of the cyclone warm conveyer belt, which also moves this heat poleward and out of the forcing region.

### 3.5 Modification of Transient-Eddy Fluxes

Before diving into a quantitative analysis of changes in transient eddy statistics, it is helpful to visualize how the transient eddies look qualitatively different between the simulations at different resolutions. We therefore show snapshots of low-pressure systems passing over the Gulf Stream SST forcing region in one of the simulations at each res-
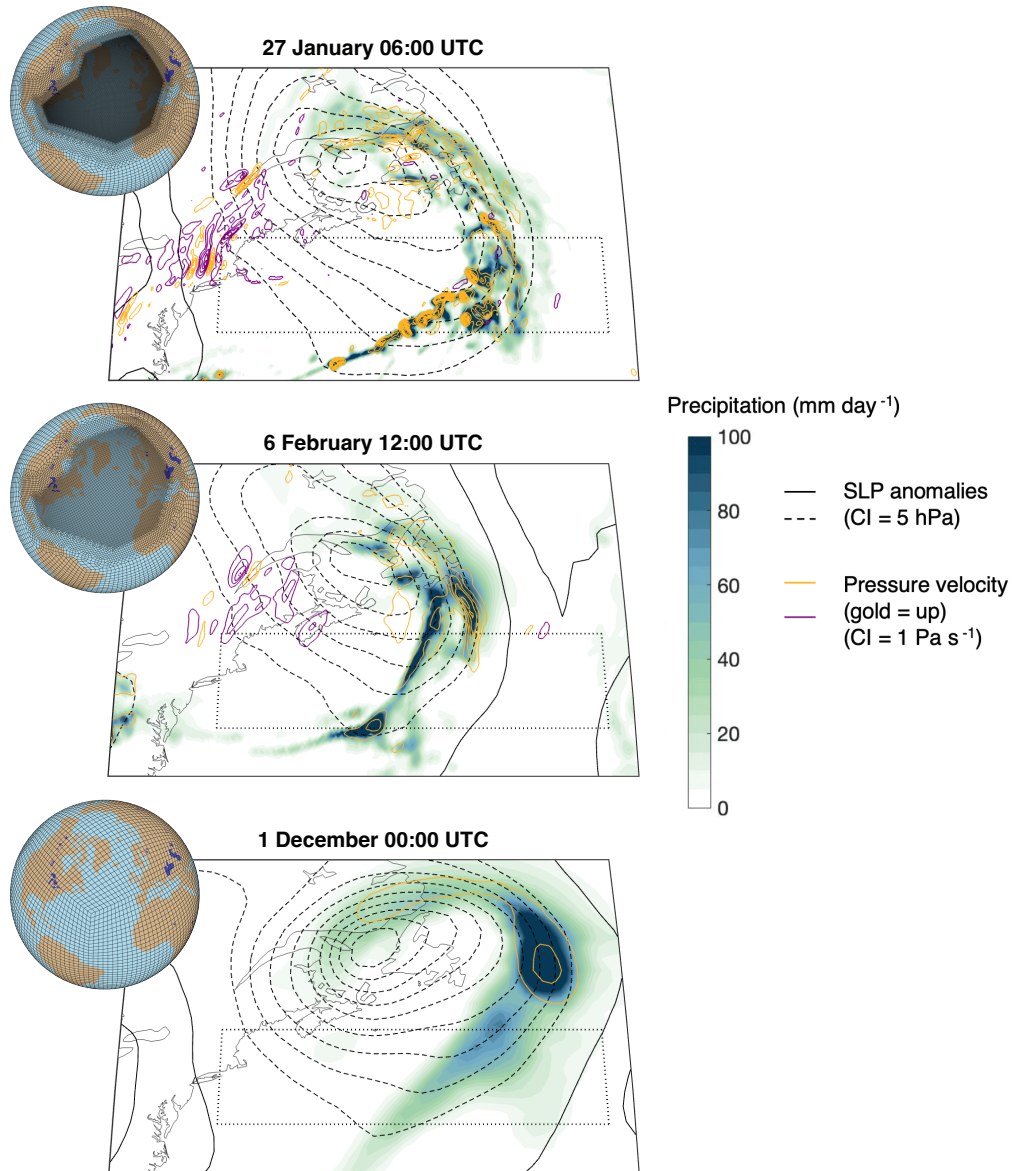
**Figure 14.** Snapshots of instantaneous total precipitation rate (shading), sea-level pressure (SLP) anomalies from the climatological mean (black contours; dashed negative), and vertical pressure velocity on the model level with average pressure of 610 hPa (gold = up; purple = down) from the WARM experiment at each resolution. Qualitatively similar snapshots are chosen such that they have an extratropical cyclone centered in the Gulf of St. Lawrence, north of the SST forcing region (thin dotted line), during winter. For plotting, precipitation and vertical velocity are interpolated to a uniform $1/8°$ grid for NATLx8 and NATLx4 and a uniform $0.7°$ grid for NE30; SLP is interpolated to the $1.25°$ longitude $\times 0.94°$ f09 grid for all simulations. The element grid is shown alongside each panel, where each element contains $3 \times 3$ independent computational grid points.
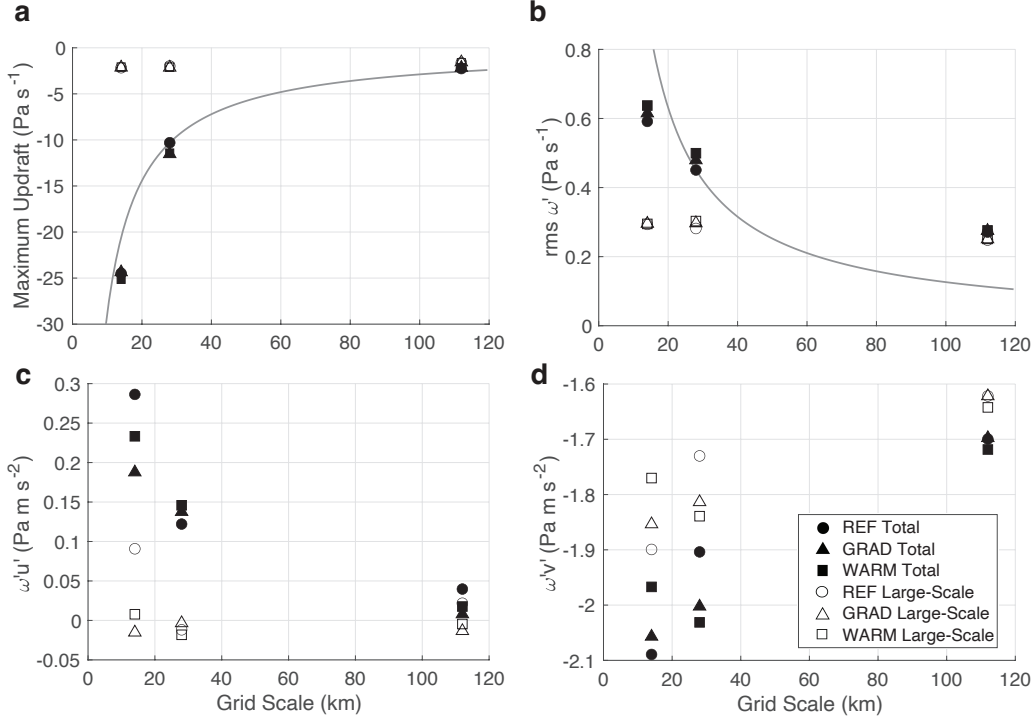
**Figure 15.** Statistics of vertical winds and vertical momentum fluxes in each simulation during DJF, computed from 6-hourly model output and plotted against the horizontal grid scale of the simulations. Statistics are computed over the southern part of the forcing region (42-72°W; 38-41°N) on the model level with average pressure of 610 hPa. (a) Temporal median of the seasonal maximum (instantaneous) updraft speed over the forcing region, expressed in pressure velocity. (b) Root-mean-square temporal variance of vertical pressure velocity over the forcing region. (c,d) Vertical fluxes of (c) zonal and (d) meridional momentum, i.e., the covariance of pressure velocity anomalies with zonal and meridional wind anomalies. In all panels, open symbols show statistics computed from large-scale fields, after interpolation to the 2.5°×1.9° f19 grid, such that variations on scales smaller than ~200 km are excluded, whereas solid symbols show the statistics computed on the native grid. Here and in Figs. 16-20, statistics are computed over 30 years in NATLx8 and NATLx4, 50 years in NE30-REF and NE30-WARM, and 48 years in NE30-GRAD (due to missing 6-hourly data). Grey lines in (a) and (b) show the $W \propto D^{-1}$ scaling, with constants chosen to intersect NATLx4-REF.

olution (Fig. 14). The highest resolution NATLx8 shows precipitation organized in frontal bands, and there is a well defined cold front with vertical velocities exceeding 10 Pa s$^{-1}$. There are also resolved gravity waves apparent in the vertical velocities in the cold sector of the cyclone. NATLx4 shows these same basic features but with muted vertical velocities, especially in the cold front. In comparison to these higher resolution simulations, precipitation and vertical velocity in the lower resolution NE30 simulations look much more blobular, without well-defined mesoscale features. This section will quantify how the large differences in the magnitude and spatial structure of vertical velocities within midlatitude cyclones influence transient eddy statistics and help shape the large-scale circulation response.

The maximum updraft velocities over the Gulf Stream increase with increased resolution according to the $W \propto D^{-1}$ scaling derived in Jeevanjee and Romps (2016) (black

lines in Fig. 15a), where $W$ is the vertical velocity scale and $D$ is the horizontal scale of convective updrafts. This is consistent with Herrington and Reed (2018), who showed that this scaling applies across different resolutions of CESM. The reason for this scaling is that buoyancy anomalies develop on smaller scales as the grid scale is reduced and this means that an equivalent buoyancy anomaly will be resisted by a narrower column of air. We actually find that the increase in updraft velocities in our simulations slightly exceeds this scaling (Fig. 15a). As was apparent in Fig. 14, these updrafts occur in mesoscale fronts, and there is therefore little change in the magnitude of large-scale updrafts (open symbols in Fig. 15a). Here, we compute large-scale statistics based on model output that has been conservatively remapped to the ∼200-km f19 grid, whereas the full-field statistics (filled symbols in Fig. 14) are computed on the native grid. The vertical velocity variance increases more slowly with resolution than the maximum updraft velocity (Fig. 15b; cf. Fig. 15a), because the area in which the strongest updrafts are occurring reduces with increased resolution. The large-scale vertical velocity variance does increase between NE30 and NATLx4, but most of the vertical velocity variance changes come from scales smaller than 200 km.

In the following discussion of changes in transient eddy fluxes, it is worth bearing in mind that transient eddies include not only synoptic motions and low-frequency variability, as is normally the case in analysis of GCM output, but they also include mesoscale motions such as slantwise convection. Studies based on reanalysis have found evidence that slantwise convection occurs over the Gulf Stream, especially in winter (Korty & Schneider, 2007; Czaja & Blunt, 2011; Sheldon & Czaja, 2014). To quantify the presence of mesoscale shear instabilities such as conditional symmetric instability in our simulations, we examine the vertical momentum fluxes by mesoscale eddies (less than 200 km scales, cf. Sheldon et al. (2017)). The vertical flux of zonal momentum by mesoscale motions (difference between open symbols and closed symbols in Fig. 15c) is positive (downwards) and increases strongly with increasing resolution, indicating a mesoscale shear instability is present that acts to weaken the mean shear, and that it becomes much more active at higher resolution. The vertical flux of meridional momentum by mesoscale motions (difference between open symbols and closed symbols in Fig. 15d) also increases strongly in magnitude with resolution, but it is negative (upwards), which is an up-gradient flux, because the Gulf Stream is a region of positive shear in the meridonal wind.

Returning to our discussion of the thermodynamic equation, the massive increases in vertical velocities with resolution has only a minor influence on the vertical EHF, because the increase in vertical velocities is primarily occurring at scales much smaller than the $O(1000$ km) scale of most temperature anomalies. This can be seen by the similarity of the climatologies of the large-scale vertical EHF as resolution is changed (black contours in Fig. 16). There is a large increase in the mesoscale upward vertical EHF with resolution (black contours in Fig. 17); however, the mesoscale vertical EHF is an order of magnitude smaller than the large-scale vertical EHF. Here, as in Fig. 15, we are separating large-scale and mesoscale fluxes by switching the order of operations of computing the variance from the 6-hourly data and conservatively remapping to the ∼200-km f19 grid, then using Reynold's decomposition.

While the contribution of mesoscale motions to the vertical EHF is small, it offers a potential explanation for what is driving the deep temperature anomaly in response to Gulf Stream SST anomalies, because the response of mesoscale vertical EHF to SST anomalies shows an upward heat flux extending into the upper troposphere in NATLx4 and NATLx8 (Fig. 17). While small in magnitude, this vertical EHF creates a direct link between the surface and the upper troposphere over the Gulf Stream. The large-scale vertical EHF response of opposite sign (Fig. 16) can be thought of as a response to the deep temperature anomaly and acts opposite to the mesoscale vertical EHF. However, both NATLx4 and NATLx8 show upward heat flux anomalies of comparable magnitude and vertical extent (Fig. 17), so why don't the NATLx4 simulations also show a deep
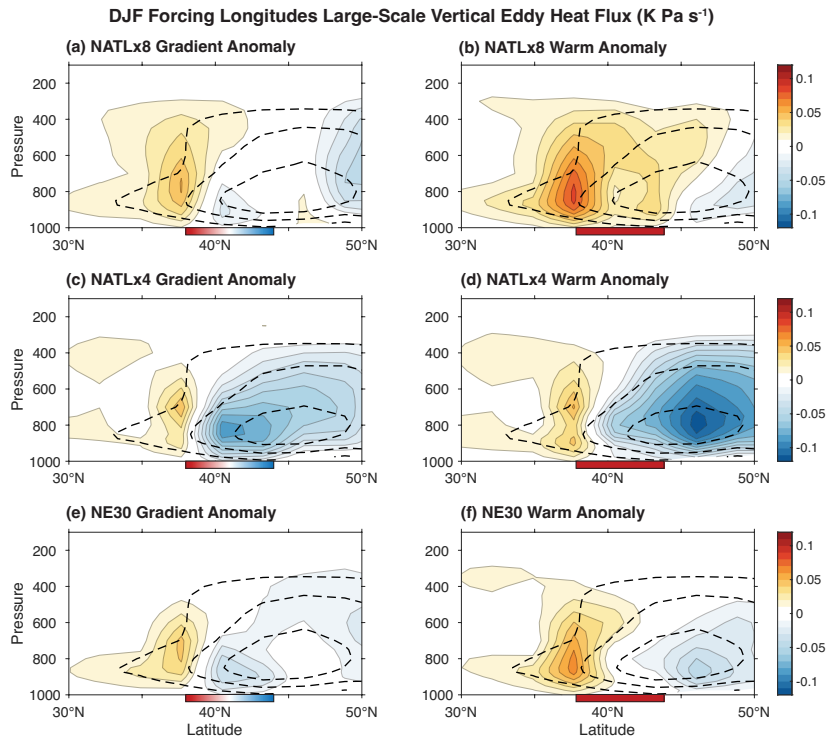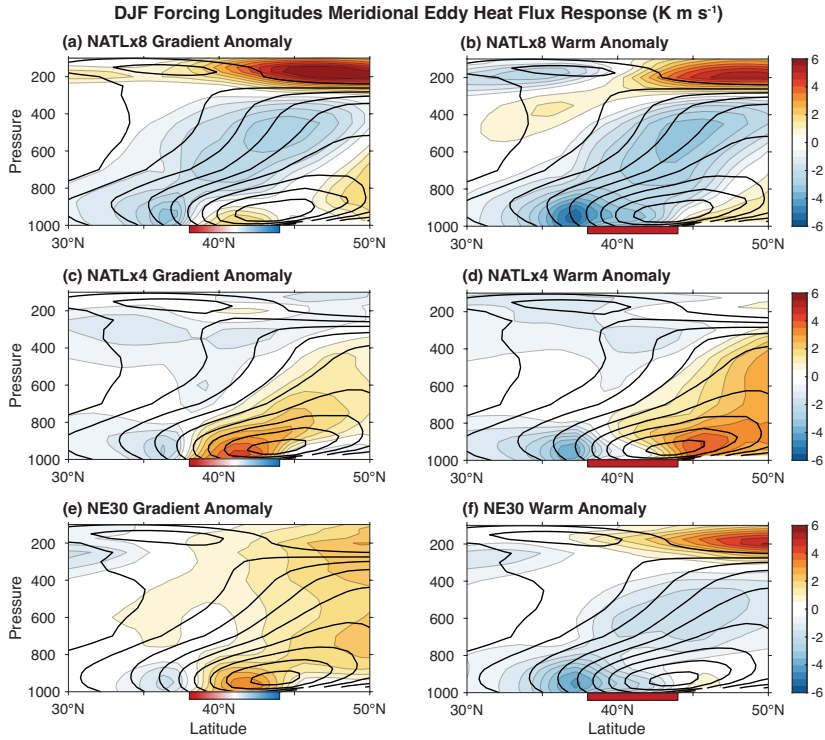
**Figure 16.** Same as Fig. 5, but for the DJF vertical eddy heat flux by large-scale motions, defined by the covariance of pressure velocity and temperature on scales greater than 200 km, computed as described in the text. Upward heat fluxes are negative. The contour interval for the climatology is 0.2 K Pa s$^{-1}$.

**DJF Forcing Longitudes Mesoscale Vertical Eddy Heat Flux (K Pa s⁻¹)**
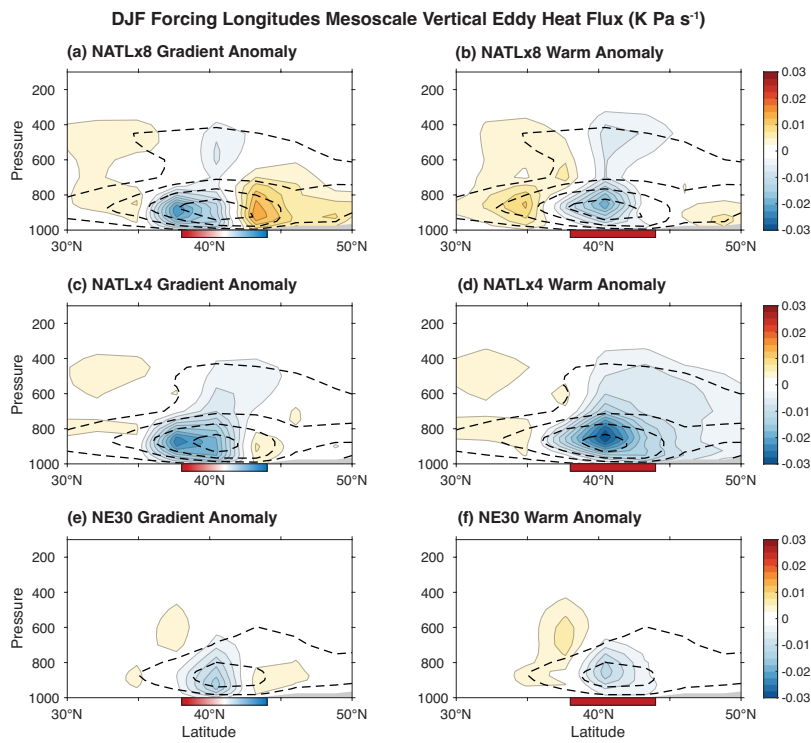
**Figure 17.** Same as Fig. 5, but for the DJF vertical eddy heat flux by mesoscale motions, defined by the covariance of pressure velocity and temperature on scales less than 200 km, computed as described in the text. Upward heat fluxes are negative. The contour interval for the climatology is 0.03 K Pa s$^{-1}$.

**Figure 18.** Same as Fig. 5, but for the DJF meridional eddy heat flux (total of large scale and mesoscale, the latter of which is negligible). The contour interval for the climatology is 5 K m s$^{-1}$.

temperature anomaly? A potential reason is that NATLx4 does not sufficiently distinguish between mesoscale and synoptic scale motions, so the upward heat fluxes from the surface become part of the cyclone warm conveyer belts, which don't just move heat upward but also poleward. This hypothesis is supported by the poleward and upward EHF by large-scale (synoptic) motions in response to SST anomalies in NATLx4 (positive anomalies north of 40°N in Figs. 18c,d and negative anomalies north of 40°N in 16c,d), unlike the EHF anomalies in NATLx8 and NE30-WARM (Figs. 18a,b,f and 16a,b,f). The differences in meridional and vertical eddy heat fluxes are also reflected in North Atlantic eddy kinetic energy (EKE), with EKE generally decreasing in NATLx8 versus shifting poleward and increasing slightly in NATLx4 (Supporting Information Fig. S6).

Drawing on the analysis presented so far, we propose a potential explanation for the difference in response between the NATLx8 and NATLx4 simulations: While effective buoyancy arguments (Jeevanjee & Romps, 2016) lead to an increase in magnitude of resolved updrafts in both NATLx4 and NATLx8 relative to NE30, this ascent is more concentrated within cold fronts (i.e., south-southeast of the cyclone center) in NATLx8 versus warm fronts (i.e., east-northeast of the cyclone center) in NATLx4 (Fig. 14). The steep isentropic slopes of cold fronts lead to an efficient pathway for surface anomalies to be communicated to the free troposphere by adiabatic motions, and the occurrence of cold fronts within the sector of the cyclone with smaller meridional winds (relative to warm fronts) means that there isn't a simultaneous poleward transport of these anomalies. This leads to a deep temperature response in NATLx8, whereas northward heat flux within the warm sector of cyclones prevents this local warm anomaly from developing in NATLx4. On the other hand, NE30-WARM also gets a deep temperature response,

albeit weaker, which we speculate comes about via parameterized convection as opposed to the resolved ascent processes that govern the NATLx4 and NATLx8 responses.

This picture can be quantitatively supported by looking at changes in the covariance of vertical velocities and meridional winds ($\omega'v'$; Fig. 15d), specifically at its response to SST anomalies. NATLx8 shows a decrease in the magnitude of $\omega'v'$ in response to SST anomalies (i.e., the black triangle and black square are less negative than the black circle). This results from a contraction of the probability distribution for the meridional wind such that more ascent occurs with weakly positive meridional winds (e.g., cold front convection) and more descent occurs with weakly negative meridional winds (e.g., in the cold sector) (Fig. 19a,b). NATLx4 shows the opposite: an increase in the magnitude of $\omega'v'$ in response to SST anomalies (Fig. 15c). While it shows a similar shift of strong ascent towards conditions with weaker meridional winds (i.e., from the warm front to the cold front) (Fig. 19c,d), it shows completely different anomalies in the weak ascent and descent parts of the joint probability distribution of $\omega$ and $v$, such that overall it shows a strengthening of the existing covariance between vertical and meridional winds more than it shows a shift in the meridional winds at which ascent and descent are occurring. Notably, NATLx4-WARM in particular shows a shift of descent from weakly negative $v$ to weakly positive $v$ (Fig. 19d), which is consistent with the ascending air becoming entrained in the poleward traveling warm conveyer belt (Browning et al., 1973), where it later descends. The response of $\omega'v'$ in NE30 is positive like in NATLx8 (Fig. 15c), but the response of the joint probability distribution of vertical and meridional wind looks different again, with a shift towards more upward and equatorward winds throughout the distribution (Fig. 19e,f).

It is not just the transient-eddy heat flux responses that show large differences with resolution. Many transient-eddy fluxes show large differences in the response to idealized SST anomalies with resolution. A notable example is the meridional flux of zonal momentum by transient eddies (Fig. 20). NATLx8 shows strong poleward anomalies in the eddy momentum flux in response to both SST anomalies, which would help to explain the strong poleward shift of the jet in these simulations (Fig. 6). It is also consistent with the negative anomalies in poleward EHF (Fig. 18) and the strong positive anomalies to the north (not shown), which from an Eliassen-Palm flux perspective should be associated with a convergence of zonal momentum, as is seen at ~45°N. The lower resolution simulations show much weaker anomalies in the meridional flux of zonal momentum by transient eddies. However, as with the thermodynamic analysis, it is difficult to disentangle the causality, i.e., whether the eddy fluxes of zonal momentum are an important reason for the large-scale circulation response or are themselves a result of the large-scale circulation response is challenging to parse out. One hint that this could be a causal factor in the response is that there is a large upward anomaly in mesoscale $\omega'u'$ (Fig. 15c) at the south edge of the $v'u'$ anomaly. Future work should investigate the momentum budget and in particular the strength of the eddy momentum flux feedback in this model configuration, because this feedback has been suggested to get stronger with higher resolution (Hardiman et al., 2022), and Fig. 20 provides some preliminary evidence of this.

## 4 Conclusions and Discussion

Our results show a large ($\sim$2 hPa $(°C)^{-1}$) East-Atlantic-intensified positive NAO-like response to warm SST anomalies south of the Gulf Stream SST front in a variable-resolution version of CAM6 with 14-km regional grid refinement over the North Atlantic. This response is weaker and has a different spatial structure in lower resolution simulations, including in simulations with 28-km regional grid refinement over the North Atlantic, corresponding to the resolution used in many previous high-resolution modeling efforts (Haarsma et al., 2016; Chang et al., 2020). The key circulation responses to SST anomalies are tabulated across the different resolutions of our simulations in Table 1. The
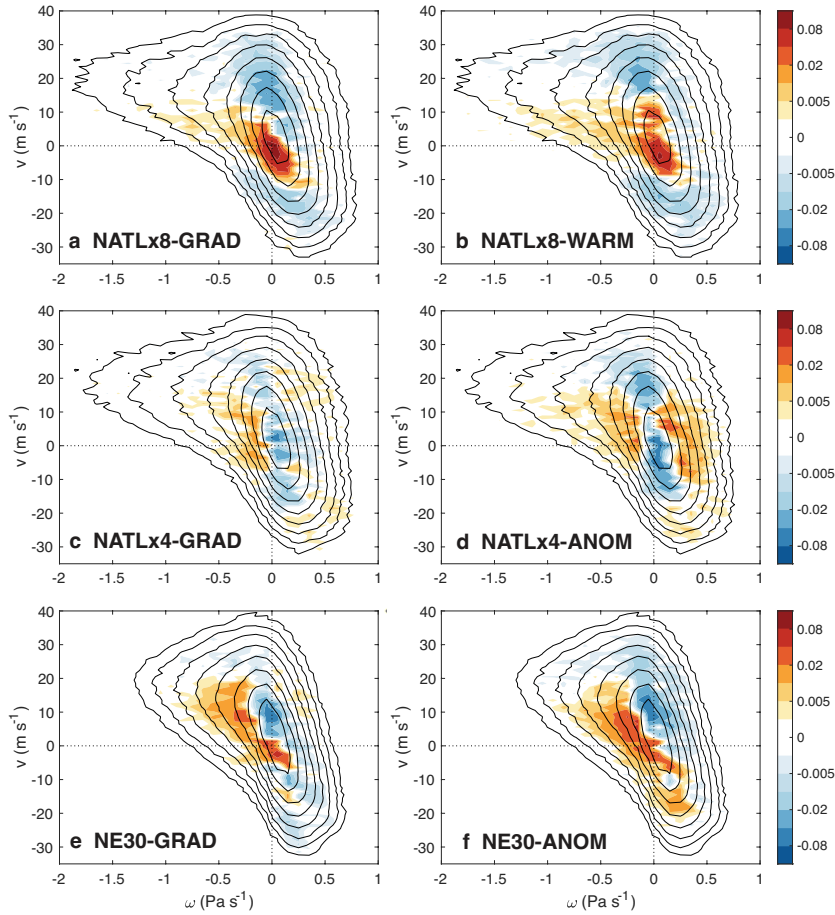
**Figure 19.** Normalized bivariate probability distributions of 6-hourly instantaneous meridional wind $v$ and vertical pressure velocity $\omega$ within the Gulf Stream forcing region during DJF, on the model level with average pressure of 610 hPa. Contours show the climatology (REF), with contour intervals [0.005 0.01 0.02 0.04 0.08 0.16 0.32 0.64]. Shading shows the response to (left) SST gradient anomalies in the Gulf Stream (GRAD−REF) and (right) warm SST anomalies in the Gulf Stream (WARM−REF) on a log scale. 3 different configurations of CAM-SE are shown: (a),(b) NATLx8, with 14-km resolution in the North Atlantic, (c),(d) NATLx4, with 28-km resolution in the North Atlantic, and (e),(f) NE30, with global 111-km resolution. This analysis is based on data that has been regridded to the 100-km f09 analysis grid, such that it does not capture the magnitude of the strongest updrafts found in NATLx4 and NATLx8.
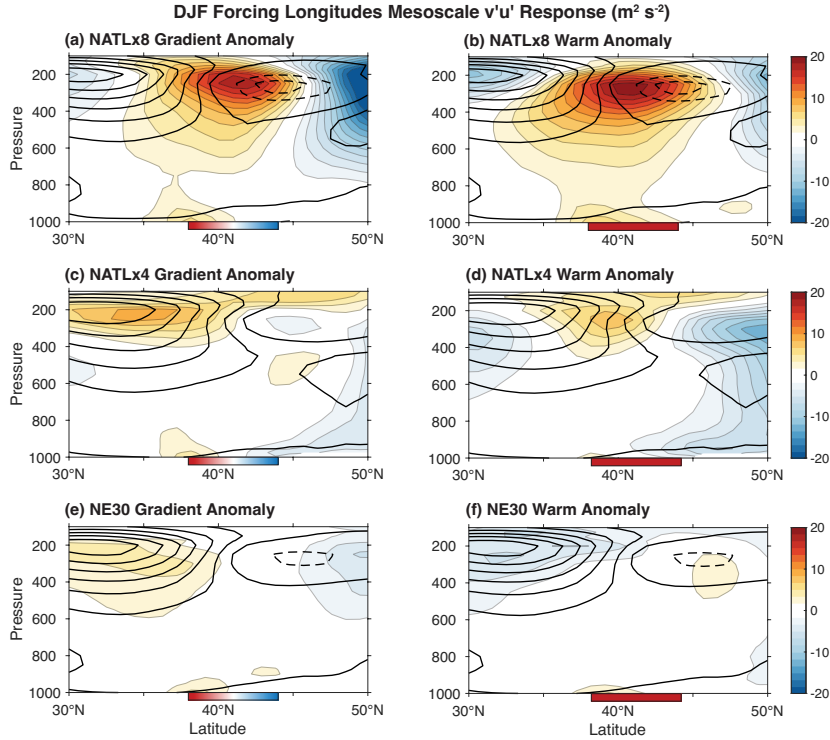
**Figure 20.** Same as Fig. 5, but for the DJF meridional eddy flux of zonal momentum (total of large scale and mesoscale, the latter of which is negligible). The contour interval for the climatology is 8 m$^2$ s$^{-2}$.

larger circulation response in NATLx8 is particularly apparent in the negative SLP and Z300 anomalies and in the zonal-mean jet shift (i.e., [U300]). The differences we find in the large-scale circulation response result entirely from differences in horizontal atmospheric resolution, because the same 1° resolution SSTs are specified at each atmospheric resolution, and the vertical resolution is kept constant. Investigating how these responses are modified by higher vertical resolution or ocean resolution is a promising avenue for future research.

### 4.1 Comparison with Observations

Given that our results are entirely based on a single atmospheric model (CAM6), it is important to validate the response found in the high resolution simulations against observations. We chose the Gulf Stream SST forcing region for our simulations based on the observational analysis of S. M. Wills et al. (2016), making this study the clearest reference point. For a peak SST anomaly amplitude of 1°C in this region, they find a 1000-hPa geopotential height response of ∼14 meters, corresponding to an SLP response of ∼1.7 hPa at a near-surface density of 1.25 kg m$^{-3}$. This is in good agreement with the 1.9 hPa (°C)$^{-1}$ found in our NATLx8 simulations (Table 1), especially considering that in the observational composite the SSTs only have a peak amplitude of 1°C and the average over the Gulf Stream region is lower than this. However, the spatial pattern of the response is quite different between NATLx8-WARM and the observational analogue of S. M. Wills et al. (2016). Where NATLx8-WARM shows a weak high over the mid-latitude North Atlantic and a strong low over the Norwegian Sea, the observational analogue shows a weak low over the Gulf Stream, a strong high over the subpolar North At-

**Table 1.** Responses of key processes and circulation indices to GRAD and WARM SST anomalies for each resolution. The largest response for each SST anomaly is highlighted in bold.

| Index | NATLx8 (14 km) | | NATLx4 (28 km) | | NE30 (110 km) | |
|---|---|---|---|---|---|---|
| | GRAD | WARM | GRAD | WARM | GRAD | WARM |
| EOF-1 NAO[a] | 0.41 | **0.44** | **0.52** | 0.42 | -0.12 | 0.35 |
| EOF-2[a] | **0.21** | **0.61** | 0.15 | -0.15 | 0.13 | 0.14 |
| SLP (hPa)[b] | 2.0, **-3.5** | 1.1, **-3.9** | **2.4**, -2.5 | **2.3**, -2.9 | 1.1, -0.72 | 1.5, -2.2 |
| Z300 (m)[b] | 30, **-41** | 24, **-47** | **33**, -28 | **28**, -29 | 14, -9.1 | 28, -24 |
| U700 (m s$^{-1}$)[b] | **1.9** | **2.1** | **1.9** | 1.8 | 0.49 | 1.4 |
| [U300] (m s$^{-1}$)[c] | **2.0**, -1.3 | **2.4**, -1.8 | 1.6, **-1.3** | 0.89, -0.50 | 0.78, -0.63 | 1.2, -0.86 |
| Near-Surface Convergence (10$^{-6}$ s$^{-1}$)[d] | 4.33 | 5.12 | **5.04** | **5.35** | 4.16 | 4.91 |
| Precipitation (mm day$^{-1}$)[d] | **1.61** | 1.89 | **1.61** | **2.23** | 1.28 | 1.87 |
| Sfc. Heat Flux (W m$^{-2}$)[d] | 88 | 91 | **105** | **117** | 93 | 113 |
| $-\partial T/\partial y$ (°C (1000 km)$^{-1}$)[d] | 0.76, **-0.92** | 1.2, **-1.3** | **1.1**, -0.36 | **1.4**, -0.71 | 0.56, -0.76 | 0.85, -1.0 |
| $\theta_{300\text{-}800}$[e] | **0.51** | **0.69** | 0.21 | 0.15 | 0.20 | 0.36 |

[a] Mean anomalies in the PCs from Figure 7 in units of interannual standard deviations.

[b] Max and min computed over 40°W-60°E in the Northern Hemisphere.

[c] Max and min over 20-70°N of the values in Figure 6.

[d] Max (and min for $-\partial T/\partial y$) computed over 30-80°W and 30-50°N.

[e] Max over 30-55°N of the 300-800 hPa vertical-average potential temperature anomaly.

lantic, and a weak low over Scandinavia and Northern Europe, more similar to the NATLx4-WARM response.

Rather than indicating a clear failure of the model, the differences in spatial pattern between the NATLx8-WARM response and the observational analogue (S. M. Wills et al., 2016) reflect differences in the associated SST pattern. The Gulf Stream SST index analyzed by S. M. Wills et al. (2016) corresponds to variability in the latitude of the Gulf Stream (see also Famooss Paolini et al., 2022), with warm SSTs north of the Gulf Stream front corresponding to a more northerly Gulf Stream position. The SST pattern used in our simulations also includes warm SST anomalies south of the Gulf Stream front, which are found to be key to the large-scale circulation response (as indicated by the similarity of the responses in the GRAD and WARM experiments). Therefore, while the SST anomalies used in our simulations help to identify which aspects of the SST pattern matter (i.e., the SSTs south of the Gulf Stream front in our simulations), they do not have a clear analogue in observed variability. For this reason, we plan to follow up on this work with simulations forced by SST patterns derived from observed variability, with the aim of making a clearer observational validation of the large-scale circulation response.

## 4.2 Mechanistic Understanding

The increased large-scale circulation response to Gulf Stream SST anomalies at high (14-km) resolution stems from an increase in resolved vertical motions within midlatitude cyclones. The increase in vertical motion within midlatitude cyclones modifies transient-eddy fluxes of energy and momentum, especially their response to SST perturbations. In the highest (14-km) resolution simulations, mesoscale motions move anomalous heat from the surface into the free troposphere, where they help to sustain a temperature anomaly throughout the free troposphere over the Gulf Stream. Our results suggest that this is mostly due to convection in the cold sector, consistent with the mechanisms discussed by Vannière et al. (2017) in the context of an individual storm system.

Simulations with a lower resolution of 28 km, which is still high by climate modeling standards, show a qualitatively different response across many variables. Based on our analyses, we suggest that this is because at this resolution the upward heat transport by mesoscale circulations becomes part of the warm-conveyer belt, where warm moist air ascends and moves poleward in the warm sector of the cyclone. In this way the signal from the surface anomalies doesn't ascend to the upper troposphere within the forcing region, but is instead moved poleward within the storm track. More work on the eddy-mean flow interactions in mesoscale-resolving models (especially those downstream in the East Atlantic) is needed to understand why this impact on the eddy heat flux does not translate into as large of an impact on the upper-tropospheric circulation. More generally, a key next step in future work should be determining how the eddy-mean flow feedback changes across this hierarchy of resolutions.

In determining how strong extratropical cyclones get and where they propagate and break (thus determining their influence on the mean flow), another mechanism that should be considered is that at high resolution the latent heating could become more concentrated in fronts, which could cause more intense cyclones that propagate further poleward (Schemm, 2023). This mechanism, investigated by Schemm (2023) in idealized variable resolution simulations of the response to midlatitude SSTs, could operate in addition to the mesoscale vertical heat transport mechanisms we investigate in this paper, and both could be important in understanding the large-scale circulation response. Another important mechanism that we have not considered here is the influence of better orographic resolution on North Atlantic circulation regimes (Davini et al., 2022). We focused on the eddy heat flux responses in the forcing region in this paper, because we found them to be important in explaining the differences between our 14-km and 28-km simulations.

The differences in response between our 28-km and 14-km resolution simulations suggests that increasing atmospheric resolution to resolve localized convective systems embedded in cold fronts may lead to fundamental differences in how the atmosphere responds to midlatitude surface perturbations. Variable-resolution simulations, due to their computational efficiency compared to mesoscale-resolving global simulations, offer a key tool for understanding the upscale influence of mesoscale processes on large-scale dynamics, a topic on which many open questions remain.

### 4.3 Implications

Our results have important implications for seasonal-to-decadal prediction, because they suggest that models with higher resolution than is currently used have a larger atmospheric response to North Atlantic SST anomalies, which are predictable at lead times of years to decades (Msadek et al., 2014; Meehl et al., 2014; S. G. Yeager et al., 2018; Borchert et al., 2021; S. G. Yeager et al., 2023). If this response is indeed realistic and can be reproduced with other SST patterns and within other models, then it suggests that increasing the resolution of our seasonal-to-decadal prediction models to resolve frontal-scale processes could lead to dramatic increases in skill in predicting decadal variations in the atmospheric circulation and regional climate, e.g., for predicting precipitation in Western Europe (Simpson et al., 2019). This is also relevant in the context of anthropogenic climate change, where non-uniform warming features such as the North Atlantic warming hole may elicit a larger forced atmospheric response, which may help to explain model-observations discrepancies in long-term circulation trends (Blackport & Fyfe, 2022; Vautard et al., 2023).

A larger response to North Atlantic SST anomalies also offers a potential resolution to the signal-to-noise paradox (Eade et al., 2014; Scaife & Smith, 2018; D. M. Smith et al., 2020): current climate models are predicting something like the correct pattern and phasing of atmospheric responses to SST anomalies but with too weak amplitude (e.g., NE30-WARM response vs. NATLx8-WARM response in Fig. 3) such that the amplitude of the predictable signal is underestimated. Our results suggest that the signal-to-noise paradox should get less severe as we increase the resolution of seasonal-to-decadal prediction models to better resolve frontal processes and their role in communicating surface anomalies into the upper troposphere. S. G. Yeager et al. (2023) have already found evidence of this in other regions in a high resolution decadal prediction system using CESM with a 0.25° atmospheric resolution and a 0.1° ocean resolution. While the 2× increase in circulation responses from 110-km to 14-km resolution in our simulations (and less than that for the NAO, see Table 1) is less than the factor or ∼4 by which some studies (e.g., D. M. Smith et al. (2020)) suggest the predictable NAO signal is underestimated, there are several factors that could explain the remainder of the discrepancy: (1) there is substantial uncertainty in the factor by which the predictable signal is underestimated, due to the short observational record, and it could in fact be less than 4, (2) other SST patterns besides the ones considered here could be more important for the difference in the (e.g., NAO) response with resolution, and (3) the response could increase further with even higher resolution or when coupled to a higher resolution ocean. It is also worth noting that an increase in eddy-mean flow feedback at higher resolution, as suggested by Hardiman et al. (2022), could increase the predictable signal independently of SST forcing.

A larger atmospheric response to North Atlantic SST anomalies would mean a larger feedback of the ocean state onto the further evolution of the SST anomalies. The details of how this influences the atmosphere-ocean dynamics of decadal variability depends on the sign and pattern of atmospheric response to realistic SST anomaly patterns, which should be investigated in future work with mesoscale-resolving climate models. However, if the atmospheric circulation response to realistic SST patterns is such as to further am-

plify those SST patterns, this could further increase the amplitude of predictable mid-latitude signals.

## 5 Open Research

The CESM2.2 run scripts, grid files, and SST forcing files used to run our simulations are available in a Zenodo repository (Jnglin Wills, 2024). The Zenodo repository also contains model output used in the paper including (1) the DJF climatology of all atmospheric fields for each simulation, (2) monthly-mean SLP for all months, (3) pentadal-mean SLP and zonal wind at 850 hPa in the North Atlantic domain, and (4) climatological covariances processed from 6-hourly model output needed for the separation of fluxes into large-scale ($> 200$ km) and mesoscale ($< 200$ km) components as described in the text. All output in the repository has been regridded to the f09 or f19 grids. Finally, the Zenodo repository also contains the MATLAB scripts needed to reproduce all analyses.

## References

Årthun, M., Wills, R. C. J., Johnson, H. L., Chafik, L., & Langehaug, H. R. (2021). Mechanisms of decadal North Atlantic climate variability and implications for the recent cold anomaly. *Journal of Climate*, *34*(9), 3421–3439.

Athanasiadis, P. J., Ogawa, F., Omrani, N.-E., Keenlyside, N., Schiemann, R., Baker, A. J., ... others (2022). Mitigating climate biases in the midlatitude North Atlantic by increasing model resolution: SST gradients and their relation to blocking and the jet. *Journal of Climate*, *35*(21), 6985–7006.

Bacmeister, J. T., Wehner, M. F., Neale, R. B., Gettelman, A., Hannay, C., Lauritzen, P. H., ... Truesdale, J. E. (2014). Exploratory high-resolution climate simulations using the Community Atmosphere Model (CAM). *Journal of Climate*, *27*(9), 3073–3099.

Beljaars, A., Brown, A., & Wood, N. (2004). A new parametrization of turbulent orographic form drag. *Quarterly Journal of the Royal Meteorological Society*, *130*(599), 1327–1347. doi: 10.1256/qj.03.73

Blackport, R., & Fyfe, J. C. (2022). Climate models fail to capture strengthening wintertime North Atlantic jet and impacts on Europe. *Science Advances*, *8*(45), eabn3112.

Bogenschutz, P. A., Gettelman, A., Morrison, H., Larson, V. E., Craig, C., & Schanen, D. P. (2013). Higher-order turbulence closure and its impact on climate simulations in the community atmosphere model. *Journal of Climate*, *26*(23), 9655–9676.

Borchert, L. F., Menary, M. B., Swingedouw, D., Sgubin, G., Hermanson, L., & Mignot, J. (2021). Improved decadal predictions of North Atlantic subpolar gyre SST in CMIP6. *Geophysical Research Letters*, *48*(3). doi: 10.1029/2020GL091307

Botev, Z. I., Grotowski, J. F., & Kroese, D. P. (2010). Kernel density estimation via diffusion. *Annals of Statistics*, *38*(5), 2916–2957. doi: 10.1214/10-AOS799

Browning, K., Hardman, M., Harrold, T., & Pardoe, C. (1973). The structure of rainbands within a mid-latitude depression. *Quarterly Journal of the Royal Meteorological Society*, *99*(420), 215–231.

Buizza, R., Bidlot, J.-R., Wedi, N., Fuentes, M., Hamrud, M., Holt, G., & Vitart, F. (2007). The new ECMWF VAREPS (variable resolution ensemble prediction system). *Quarterly Journal of the Royal Meteorological Society: A Journal of the Atmospheric Sciences., applied meteorology and physical oceanography*, *133*(624), 681–695.

Canuto, C., Hussaini, M. Y., Quarteroni, A., & Zang, T. (2007). *Spectral methods: Evolution to complex geometries and applications to fluid dynamics* (1st ed.). Springer.

Chang, P., Zhang, S., Danabasoglu, G., Yeager, S. G., Fu, H., Wang, H., . . . Wu, L. (2020). An unprecedented set of high-resolution earth system simulations for understanding multiscale interactions in climate variability and change. *Journal of Advances in Modeling Earth Systems*, *12*(12), e2020MS002298.

Chelton, D. B., Esbensen, S. K., Schlax, M. G., Thum, N., Freilich, M. H., Wentz, F. J., . . . Schopf, P. S. (2001). Observations of coupling between surface wind stress and sea surface temperature in the eastern tropical Pacific. *Journal of Climate*, *14*(7), 1479–1498.

Computational and Information Systems Laboratory. (2019). *Cheyenne: Hpe/sgi ice xa system (university community computing).* Boulder, CO: National Center for Atmospheric Research. doi: 10.5065/D6RX99HX

Czaja, A., & Blunt, N. (2011). A new mechanism for ocean–atmosphere coupling in midlatitudes. *Quarterly Journal of the Royal Meteorological Society*, *137*(657), 1095–1101.

Czaja, A., & Frankignoul, C. (1999). Influence of the North Atlantic SST on the atmospheric circulation. *Geophysical Research Letters*, *26*(19), 2969–2972.

Czaja, A., & Frankignoul, C. (2002). Observed impact of Atlantic SST anomalies on the North Atlantic Oscillation. *Journal of Climate*, *15*(6), 606–623.

Czaja, A., Frankignoul, C., Minobe, S., & Vannière, B. (2019). Simulating the midlatitude atmospheric circulation: What might we gain from high-resolution modeling of air-sea interactions? *Current Climate Change Reports*, *5*(4), 390–406.

Danabasoglu, G., Lamarque, J., Bacmeister, J., Bailey, D. A., DuVivier, A. K., Edwards, J., . . . Strand, W. G. (2020). The Community Earth System Model version 2 (CESM2). *Journal of Advances in Modeling Earth Systems*, *12*(2). doi: 10.1029/2019MS001916

Danielson, J. J., & Gesch, D. B. (2011). *Global multi-resolution terrain elevation data 2010 (GMTED2010)* (Open File Rep. No. 2011-1073). US Geological Survey. doi: https://doi.org/10.3133/ofr20111073

Davini, P., Fabiano, F., & Sandu, I. (2022). Orographic resolution driving the improvements associated with horizontal resolution increase in the Northern Hemisphere winter mid-latitudes. *Weather and Climate Dynamics*, *3*(2), 535–553.

Delworth, T. L., Zeng, F., Zhang, L., Zhang, R., Vecchi, G. A., & Yang, X. (2017). The central role of ocean dynamics in connecting the North Atlantic Oscillation to the extratropical component of the Atlantic multidecadal oscillation. *Journal of Climate*, *30*(10), 3789–3805.

Deser, C., & Blackmon, M. L. (1993). Surface climate variations over the North Atlantic Ocean during winter: 1900–1989. *Journal of Climate*, *6*(9), 1743–1753.

Dorrington, J., Strommen, K., & Fabiano, F. (2022). Quantifying climate model representation of the wintertime Euro-Atlantic circulation using geopotential-jet regimes. *Weather and Climate Dynamics*, *3*(2), 505–533.

Eade, R., Smith, D., Scaife, A., Wallace, E., Dunstone, N., Hermanson, L., & Robinson, N.    (2014).    Do seasonal-to-decadal climate predictions underestimate the predictability of the real world?    *Geophysical Research Letters*, *41*(15), 5620–5628.

Famooss Paolini, L., Athanasiadis, P. J., Ruggieri, P., & Bellucci, A.    (2022).    The atmospheric response to meridional shifts of the Gulf Stream SST front and its dependence on model resolution.    *Journal of Climate*, *35*(18), 6007–6030.    doi: 10.1175/JCLI-D-21-0530.1

Frankignoul, C., de Coëtlogon, G., Joyce, T. M., & Dong, S.    (2001).    Gulf Stream variability and ocean–atmosphere interactions.    *Journal of Physical Oceanography*, *31*(12), 3516–3529.

Gastineau, G., D'Andrea, F., & Frankignoul, C. (2013). Atmospheric response to the North Atlantic Ocean variability on seasonal to decadal time scales.    *Climate Dynamics*, *40*(9-10), 2311–2330.

Gastineau, G., & Frankignoul, C.    (2015).    Influence of the North Atlantic SST variability on the atmospheric circulation during the twentieth century.    *Journal of Climate*, *28*(4), 1396–1416.

Gettelman, A., Hannay, C., Bacmeister, J. T., Neale, R. B., Pendergrass, A., Danabasoglu, G., ... others    (2019).    High climate sensitivity in the Community Earth System Model version 2 (CESM2).    *Geophysical Research Letters*, *46*(14), 8329–8337.

Gettelman, A., & Morrison, H. (2015). Advanced two-moment bulk microphysics for global models. Part I: off-line tests and comparison with other schemes.    *Journal of Climate*, *28*(3), 1268–1287.

Gettelman, A., Morrison, H., Santos, S., Bogenschutz, P., & Caldwell, P.    (2015).    Advanced two-moment bulk microphysics for global models. Part II: global model solutions and aerosol–cloud interactions.    *Journal of Climate*, *28*(3), 1288–1307.

Golaz, J.-C., Larson, V. E., & Cotton, W. R.  (2002).  A pdf-based model for boundary layer clouds. Part I: method and model description.    *Journal of the Atmospheric Sciences*, *59*(24), 3540–3551.    doi: 10.1175/1520-0469(2002)059⟨3540: apbmfb⟩2.0.co;2

Guba, O., Taylor, M. A., Ullrich, P. A., Overfelt, J. R., & Levy, M. N.    (2014).    The spectral element method (SEM) on variable-resolution grids: evaluating grid sensitivity and resolution-aware numerical viscosity.    *Geosci. Model Dev.*, *7*(6), 2803–2816. doi: 10.5194/gmd-7-2803-2014

Haarsma, R. J., Roberts, M. J., Vidale, P. L., Senior, C. A., Bellucci, A., Bao, Q., ... von Storch, J.-S.    (2016).    High resolution model intercomparison project (HighResMIP v1.0) for CMIP6.    *Geoscientific Model Development*, *9*(11), 4185–4208.

Hardiman, S. C., Dunstone, N. J., Scaife, A. A., Smith, D. M., Comer, R., Nie, Y., & Ren, H.-L.  (2022).  Missing eddy feedback may explain weak signal-to-noise ratios in climate predictions. *npj Climate and Atmospheric Science*, *5*(1), 57.

Hayes, S., McPhaden, M., & Wallace, J.    (1989).    The influence of sea-surface temperature on surface wind in the eastern equatorial Pacific: Weekly to monthly variability. *Journal of Climate*, *2*(12), 1500–1506.

Herrington, A. R., Lauritzen, P. H., Lofverstrom, M., Lipscomb, W. H., Gettelman, A., & Taylor, M. A.    (2022).    Impact of grids and dynamical cores in CESM2.2 on the surface mass balance of the Greenland ice sheet.    *Journal of Advances in Modeling Earth Systems*, *14*(11), e2022MS003192.    doi: 10.1029/2022MS003192

Herrington, A. R., & Reed, K. A.    (2018).    An idealized test of the response of the Community Atmosphere Model to near-grid-scale forcing across hydrostatic resolutions.    *Journal of Advances in Modeling Earth Systems*, *10*(2), 560–575. doi: 10.1002/2017MS001078

Herrington, A. R., & Reed, K. A. (2020). On resolution sensitivity in the Community Atmosphere Model. *Quarterly Journal of the Royal Meteorological Society*, *146*(733), 3789–3807. doi: 10.1002/qj.3873

Hersbach, H., Bell, B., Berrisford, P., Hirahara, S., Horányi, A., Muñoz-Sabater, J., ... Thépaut, J.-N. (2020). The ERA5 global reanalysis. *Quarterly Journal of the Royal Meteorological Society*, *146*(730), 1999-2049.

Hoskins, B. J., & Karoly, D. J. (1981). The steady linear response of a spherical atmosphere to thermal and orographic forcing. *Journal of the Atmospheric Sciences.*, *38*(6), 1179–1196.

Hurrell, J. W., Hack, J. J., Shea, D., Caron, J. M., & Rosinski, J. (2008). A new sea surface temperature and sea ice boundary dataset for the Community Atmosphere Model. *Journal of Climate*, *21*(19), 5145–5153.

Jeevanjee, N., & Romps, D. M. (2016). Effective buoyancy at the surface and aloft: Effective buoyancy. *Quarterly Journal of the Royal Meteorological Society*, *142*(695), 811–820. doi: 10.1002/qj.2683

Jnglin Wills, R. (2024). Zenodo Repository for "Resolving weather fronts increases the large-scale circulation response to Gulf Stream SST anomalies in variable-resolution CESM2 simulations" [Software]. Zenodo. doi: https://doi.org/10.5281/zenodo.11172058

Kaspi, Y., & Schneider, T. (2011). Downstream self-destruction of storm tracks. *Journal of the Atmospheric Sciences*, *68*(10), 2459–2464.

Korty, R. L., & Schneider, T. (2007). A climatology of the tropospheric thermal stratification using saturation potential vorticity. *Journal of Climate*, *20*(24), 5977–5991.

Kushnir, Y., Robinson, W., Bladé, I., Hall, N., Peng, S., & Sutton, R. (2002). Atmospheric GCM response to extratropical SST anomalies: Synthesis and evaluation. *Journal of Climate*, *15*(16), 2233–2256.

Kuwano-Yoshida, A., Minobe, S., & Xie, S.-P. (2010). Precipitation response to the Gulf Stream in an atmospheric GCM. *Journal of Climate*, *23*(13), 3676–3698. doi: 10.1175/2010JCLI3261.1

Lau, N.-C., & Nath, M. J. (1994). A modeling study of the relative roles of tropical and extratropical SST anomalies in the variability of the global atmosphere-ocean system. *Journal of Climate*, *7*(8), 1184–1207. doi: 10.1175/1520-0442(1994)007⟨1184:AMSOTR⟩2.0.CO;2

Lauritzen, P., Bacmeister, J., Callaghan, P., & Taylor, M. (2015). NCAR_Topo (v1. 0): NCAR global model topography generation software for unstructured grids. *Geoscientific Model Development*, *8*(12), 3975–3986.

Lauritzen, P. H., Nair, R. D., Herrington, A., Callaghan, P., Goldhaber, S., Dennis, J., ... others (2018). NCAR release of CAM-SE in CESM2.0: A reformulation of the spectral element dynamical core in dry-mass vertical coordinates with comprehensive treatment of condensates and energy. *Journal of Advances in Modeling Earth Systems*, *10*(7), 1537–1570.

Lauritzen, P. H., Taylor, M. A., Overfelt, J., Ullrich, P. A., Nair, R. D., Goldhaber, S., & Kelly, R. (2017). CAM-SE-CSLAM: Consistent coupling of a conservative semi-Lagrangian finite-volume method with spectral element dynamics. *Mon. Wea. Rev.*, *145*(3), 833-855. doi: 10.1175/MWR-D-16-0258.1

Lawrence, D. M., Fisher, R. A., Koven, C. D., Oleson, K. W., Swenson, S. C., Bonan, G., ... others (2019). The community land model version 5: Description of new features, benchmarking, and impact of forcing uncertainty. *Journal of Advances in Modeling Earth Systems*, *11*(12), 4245–4287.

Lin, S.-J. (2004). A 'vertically Lagrangian' finite-volume dynamical core for global models. *Mon. Wea. Rev.*, *132*, 2293-2307.

Lindzen, R. S., & Nigam, S. (1987). On the role of sea surface temperature gradients in forcing low-level winds and convergence in the tropics. *Journal of the Atmospheric Sciences*, *44*(17), 2418–2436. doi: 10.1175/1520-0469(1987)044⟨2418:

otross⟩2.0.co;2

Liu, X., Penner, J. E., Ghan, S. J., & Wang, M. (2007). Inclusion of ice microphysics in the NCAR Community Atmospheric Model version 3 (CAM3). *Journal of Climate*, *20*(18), 4526–4547.

Meehl, G. A., Goddard, L., Boer, G., Burgman, R., Branstator, G., Cassou, C., . . . Yeager, S. (2014). Decadal climate prediction: an update from the trenches. *Bull. Am. Meteorol. Soc.*, *95*(2), 243–267.

Menary, M. B., Hodson, D. L., Robson, J. I., Sutton, R. T., & Wood, R. A. (2015). A mechanism of internal decadal Atlantic Ocean variability in a high-resolution coupled climate model. *Journal of Climate*, *28*(19), 7764–7785.

Minobe, S., Kuwano-Yoshida, A., Komori, N., Xie, S.-P., & Small, R. J. (2008). Influence of the Gulf Stream on the troposphere. *Nature*, *452*(7184), 206–209.

Msadek, R., Delworth, T., Rosati, A., Anderson, W., Vecchi, G., Chang, Y.-S., . . . others (2014). Predicting a decadal shift in North Atlantic climate variability using the GFDL forecast system. *Journal of Climate*, *27*(17), 6472–6496.

Nakamura, H., Sampe, T., Goto, A., Ohfuchi, W., & Xie, S.-P. (2008). On the importance of midlatitude oceanic frontal zones for the mean state and dominant variability in the tropospheric circulation. *Geophysical Research Letters*, *35*(15), L15709. doi: 10.1029/2008GL034010

Neale, R. B., Richter, J. H., & Jochum, M. (2008). The impact of convection on ENSO: From a delayed oscillator to a series of events. *Journal of Climate*, *21*, 5904-5924.

Oldenburg, D., Wills, R. C. J., Armour, K. C., & Thompson, L. (2022). Resolution dependence of atmosphere–ocean interactions and water mass transformation in the North Atlantic. *Journal of Geophysical Research: Oceans*, *127*(e2021JC018102). doi: 10.1029/2021JC018102

O'Reilly, C. H., Minobe, S., Kuwano-Yoshida, A., & Woollings, T. (2017). The Gulf Stream influence on wintertime North Atlantic jet variability. *Quarterly Journal of the Royal Meteorological Society*, *143*(702), 173–183. doi: 10.1002/qj.2907

O'Reilly, C. H., Minobe, S., & Kuwano-Yoshida, A. (2016). The influence of the Gulf Stream on wintertime European blocking. *Climate Dynamics*, *47*(5-6), 1545–1567. doi: 10.1007/s00382-015-2919-0

Parfitt, R., Czaja, A., Minobe, S., & Kuwano-Yoshida, A. (2016). The atmospheric frontal response to SST perturbations in the Gulf Stream region. *Geophysical Research Letters*, *43*(5), 2299–2306. doi: 10.1002/2016GL067723

Richter, J. H., & Rasch, P. J. (2008). Effects of convective momentum transport on the atmospheric circulation in the Community Atmosphere Model, version 3. *Journal of Climate*, *21*(7), 1487-1499.

Scaife, A. A., & Smith, D. (2018). A signal-to-noise paradox in climate science. *npj Climate and Atmospheric Science*, *1*(1), 1–8.

Schemm, S. (2023). Toward eliminating the decades-old "too zonal and too equatorward" storm-track bias in climate models. *Journal of Advances in Modeling Earth Systems*, *15*(2), e2022MS003482.

Seo, H., O'Neill, L. W., Bourassa, M. A., Czaja, A., Drushka, K., Edson, J. B., . . . Wang, Q. (2023). Ocean mesoscale and frontal-scale ocean–atmosphere interactions and influence on large-scale climate: A review. *Journal of Climate*, *36*(7), 1981–2013. doi: 10.1175/JCLI-D-21-0982.1

Sheldon, L., & Czaja, A. (2014). Seasonal and interannual variability of an index of deep atmospheric convection over western boundary currents. *Quarterly Journal of the Royal Meteorological Society*, *140*(678), 22–30.

Sheldon, L., Czaja, A., Vannière, B., Morcrette, C., Sohet, B., Casado, M., & Smith, D. (2017). A 'warm path' for Gulf Stream–troposphere interactions. *Tellus A: Dynamic Meteorology and Oceanography*, *69*(1), 1299397.

Simpson, I. R., Deser, C., McKinnon, K. A., & Barnes, E. A. (2018). Modeled and

observed multidecadal variability in the North Atlantic jet stream and its connection to sea surface temperatures. *Journal of Climate*, *31*(20), 8313–8338.

Simpson, I. R., Yeager, S. G., McKinnon, K. A., & Deser, C. (2019). Decadal predictability of late winter precipitation in western Europe through an ocean–jet stream connection. *Nature Geoscience*, *12*(8), 613–619.

Small, R. J., Tomas, R. A., & Bryan, F. O. (2014). Storm track response to ocean fronts in a global high-resolution climate model. *Climate Dynamics*, *43*(3-4), 805–828. doi: 10.1007/s00382-013-1980-9

Smirnov, D., Newman, M., Alexander, M. A., Kwon, Y.-O., & Frankignoul, C. (2015). Investigating the local atmospheric response to a realistic shift in the Oyashio sea surface temperature front. *Journal of Climate*, *28*(3), 1126–1147.

Smith, D., Eade, R., Scaife, A., Caron, L.-P., Danabasoglu, G., DelSole, T., ... others (2019). Robust skill of decadal climate predictions. *npj Climate and Atmospheric Science*, *2*(1), 13.

Smith, D. M., Scaife, A. A., Eade, R., Athanasiadis, P., Bellucci, A., Bethke, I., ... others (2020). North Atlantic climate far more predictable than models imply. *Nature*, *583*(7818), 796–800.

Strommen, K. (2020). Jet latitude regimes and the predictability of the North Atlantic Oscillation. *Quarterly Journal of the Royal Meteorological Society*, *146*(730), 2368–2391. doi: 10.1002/qj.3796

Strommen, K., Mavilia, I., Corti, S., Matsueda, M., Davini, P., Hardenberg, J., ... Mizuta, R. (2019). The sensitivity of Euro-Atlantic regimes to model horizontal resolution. *Geophysical Research Letters*, *46*(13), 7810–7818. doi: 10.1029/2019GL082843

Taylor, M. A., & Fournier, A. (2010). A compatible and conservative spectral element method on unstructured grids. *Journal of Computational Physics*, *229*(17), 5879 - 5895. doi: 10.1016/j.jcp.2010.04.008

Taylor, M. A., Tribbia, J., & Iskandarani, M. (1997). The spectral element method for the shallow water equations on the sphere. *J. Comput. Phys.*, *130*, 92-108.

Trenberth, K. E. (1984). Some effects of finite sample size and persistence on meteorological statistics. Part I: Autocorrelations. *Monthly Weather Review*, *112*(12), 2359–2368.

Tsopouridis, L., Spengler, T., & Spensberger, C. (2021). Smoother versus sharper Gulf Stream and Kuroshio sea surface temperature fronts: Effects on cyclones and climatology. *Weather and Climate Dynamics*, *2*(4), 953–970. doi: 10.5194/wcd-2-953-2021

van Kampenhout, L., Rhoades, A. M., Herrington, A. R., Zarzycki, C. M., Lenaerts, J., Sacks, W. J., & Broeke, M. R. (2019). Regional grid refinement in an earth system model: impacts on the simulated greenland surface mass balance. *The Cryosphere*, *13*(6), 1547–1564.

Vannière, B., Czaja, A., Dacre, H., & Woollings, T. (2017). A "cold path" for the Gulf Stream–troposphere connection. *Journal of Climate*, *30*(4), 1363–1379. doi: 10.1175/JCLI-D-15-0749.1

Vautard, R., Cattiaux, J., Happé, T., Singh, J., Bonnet, R., Cassou, C., ... others (2023). Heat extremes in Western Europe increasing faster than simulated due to atmospheric circulation trends. *Nature Communications*, *14*(1), 6803.

White, R. H., Hilgenbrink, C., & Sheshadri, A. (2019). The Importance of Greenland in Setting the Northern Preferred Position of the North Atlantic Eddy-Driven Jet. *Geophysical Research Letters*, *46*(23), 14126–14134. doi: 10.1029/2019GL084780

Wijngaard, R. R., Herrington, A. R., Lipscomb, W. H., Leguy, G. R., & An, S.-I. (2023). Exploring the ability of the variable-resolution Community Earth System Model to simulate cryospheric–hydrological variables in High Mountain Asia. *The Cryosphere*, *17*(9), 3803–3828.

Williamson, D. L. (2013). The effect of time steps and time-scales on parametriza-

tion suites. *Quarterly Journal of the Royal Meteorological Society*, *139*(671), 548–560.

Wills, R. C. J., Armour, K. C., Battisti, D. S., & Hartmann, D. L. (2019). Ocean-atmosphere dynamic coupling fundamental to the Atlantic Multidecadal Oscillation. *Journal of Climate*, *32*(1), 251–272.

Wills, S. M., Thompson, D. W., & Ciasto, L. M. (2016). On the observed relationships between variability in Gulf Stream sea surface temperatures and the atmospheric circulation over the North Atlantic. *Journal of Climate*, *29*(10), 3719–3730.

Woollings, T., Hannachi, A., & Hoskins, B. (2010). Variability of the North Atlantic eddy-driven jet stream: Variability of the North Atlantic jet stream. *Quarterly Journal of the Royal Meteorological Society*, *136*(649), 856–868. doi: 10.1002/qj.625

Yeager, S., & Robson, J. (2017). Recent progress in understanding and predicting Atlantic decadal climate variability. *Current Climate Change Reports*, *3*(2), 112–127.

Yeager, S. G., Chang, P., Danabasoglu, G., Rosenbloom, N., Zhang, Q., Castruccio, F. S., . . . Simpson, I. R. (2023). Reduced Southern Ocean warming enhances global skill and signal-to-noise in an eddy-resolving decadal prediction system. *npj Climate and Atmospheric Science*, *6*(1), 107.

Yeager, S. G., Danabasoglu, G., Rosenbloom, N. A., Strand, W., Bates, S. C., Meehl, G., . . . Lovenduski, N. S. (2018). Predicting near-term changes in the earth system: A large ensemble of initialized decadal prediction simulations using the Community Earth System Model. *Bull. Am. Meteorol. Soc.*, *99*(9), 1867–1886.

Zarzycki, C. M., & Jablonowski, C. (2014). A multidecadal simulation of Atlantic tropical cyclones using a variable-resolution global atmospheric general circulation model. *Journal of Advances in Modeling Earth Systems*, *6*(3), 805–828.

Zarzycki, C. M., Jablonowski, C., Thatcher, D. R., & Taylor, M. A. (2015). Effects of localized grid refinement on the general circulation and climatology in the Community Atmosphere Model. *Journal of Climate*, *28*(7), 2777–2803.

Zhang, G., & McFarlane, N. (1995). Sensitivity of climate simulations to the parameterization of cumulus convection in the Canadian climate centre general circulation model. *Atmosphere-Ocean*, *33*(3), 407-446.

Zhang, R., Sutton, R., Danabasoglu, G., Kwon, Y.-O., Marsh, R., Yeager, S. G., . . . Little, C. M. (2019). A review of the role of the Atlantic Meridional Overturning Circulation in Atlantic multidecadal variability and associated climate impacts. *Reviews of Geophysics*.